



Universitat Autònoma de Barcelona

## LV Contour Segmentation in TMR images using Semantic Description of Tissue and Prior Knowledge Correction

**Albert Andaluz González**

*Computer Vision Centre*

*Autonomous University of Barcelona*

*Bellaterra, 08192, Spain (EU)*

AANDALUZ@CVC.UAB.CAT

**Advisors:** Débora Gil Resina

Jaume Garcia i Barnés

DEBORA@CVC.UAB.CAT

JAUME.GARCIA@CVC.UAB.CAT

### Abstract

The Diagnosis of Left Ventricle (LV) pathologies is related to regional wall motion analysis. Health indicator scores such as the rotation and the torsion are useful for the diagnose of the Left Ventricle (LV) function. However, this requires proper identification of LV segments. On one hand, manual segmentation is robust, but it is slow and requires medical expertise. On the other hand, the tag pattern in Tagged Magnetic Resonance (TMR) sequences is a problem for the automatic segmentation of the LV boundaries. Consequently, we propose a method based in the classical formulation of parametric Snakes, combined with Active Shape models. Our semantic definition of the LV is tagged tissue that experiences motion in the systolic cycle. This defines two energy potentials for the Snake convergence. Additionally, the mean shape corrects excessive deviation from the anatomical shape. We have validated our approach in 15 healthy volunteers and two short axis cuts. In this way, we have compared the automatic segmentations to manual shapes outlined by medical experts. Also, we have explored the accuracy of clinical scores computed using automatic contours. The results show minor divergence in the approximation and the manual segmentations as well as robust computation of clinical scores in all cases. From this we conclude that the proposed method is a promising support tool for clinical analysis.

**Keywords:** Active Contour Models, Snakes, Active Shape Models, Deformable Templates, Left Ventricle Segmentation, Generalized Orthogonal Procrustes Analysis, Harmonic Phase Flow, Principal Component Analysis, Tagged Magnetic Resonance

# Contents

1	Introduction . . . . .	3
1.1	Imaging Modalities for LV Intramural Motion Estimation . . . . .	3
1.2	Left Ventricle Segmentation . . . . .	5
1.3	Main goals . . . . .	6
2	State of the Art . . . . .	7
2.1	Deformable models . . . . .	7
2.2	Segmentation of TMR images . . . . .	9
2.3	Our approach . . . . .	9
3	Our contribution . . . . .	10
3.1	Segmentation stage . . . . .	10
3.2	Shape Correction Stage . . . . .	14
3.3	TMR Segmentation . . . . .	17
4	Results . . . . .	20
4.1	Segmentation Error . . . . .	20
4.2	Accuracy of Clinical Scores . . . . .	22
5	Conclusions . . . . .	29
6	Acknowledgements . . . . .	31
	References . . . . .	35
	List of Figures . . . . .	37
	List of Tables . . . . .	38

<b>Acronyms</b>	<b>39</b>
-----------------	-----------

## 1. Introduction

Nowadays, heart diseases constitute the leading cause of mortality in developed countries. According to the World Health Organization (WHO), they already represent 30% of all global deaths. In order to address this public health concern, efficient detection programs are essential. Recent advances in medical imaging allow an intrusive deep insight of the organ anatomy and provide specific data, such as function and physiology. Most of the times, medical experts can perform a qualitative evaluation of the heart function, which, unfortunately, does not produce quantitative data with an objective clinical value. This has encouraged the development of several image processing methods for the extraction of reliable clinical scores for the diagnosis of heart diseases. These scores might be global (such as myocardial rotation and torsion) or local (such as motion and strain).

A main feature of heart diseases is that they decrease the blood supply at specific areas of the heart, leading to abnormal regional wall motion patterns. It follows that wall motion analysis is crucial for an early diagnosis. Accurate detection of regional wall motion abnormalities requires estimation of intramural (within myocardial walls) function parameters (such as rotation). Computation of function parameters for regional wall motion abnormalities assessment requires estimation of intramural motion, as well as, segmentation of myocardial boundaries.

### 1.1 Imaging Modalities for LV Intramural Motion Estimation

In order to estimate intramural motion, imaging techniques that induce landmarks inside the myocardium are required. The only imaging modalities that are well suited for non-invasive induction of landmarks are Tagged Magnetic Resonance (TMR) and Speckle Tracking Echocardiography (STE). Both induce specific features (markers) that can be used for estimating the motion of the LV. Such fields already constitute an indicator of the local function, which is used for computing other indicators, such as the strain, rotation and torsion (Pujadas et al., 2008).

Speckle Tracking Echocardiography is a recent non-invasive method for the LV regional function. It is based on the principle that scattering, reflection and interference of a ultrasonic beam over the myocardium causes speckles in the resulting image. Each speckle defines a tissue marker. Thus, during the systolic cycle these markers move and can be used for tracking (Goffinet and Vanoverschelde, 2007). Tissue velocity (Doppler) signals may be used for rotational velocity scores. However, STE is limited by the quality of the sonography (noise). Moreover, similar patient profiles may have large noise amounts, rendering STE unreliable for accurate spatial analysis (Notomi et al., 2005).

Among all current modalities for visualizing intramural motion, TMR is the reference modality. Tagged Magnetic Resonance is an extension of Magnetic Resonance Imaging (MRI), whose principles base on the dipole properties of the hydrogen atoms and their characteristic spins. Under a strong magnetic field, these atoms temporally change their own axial direction. Simultaneously, they also emit their own Radio Frequency (RF) signal which can be detected using an external coil. Thus, frequency analysis of the hydrogen atoms RF enables visual reconstruction of the tissue (Axel et al., 2005).

In order to generate the tags, TMR includes a further step that exploits the principle of magnetic saturation. The tags are generated with Radio Frequency pulse patterns (that is, the tagging pulse) combined with pulsed magnetic fields gradients. In the image domain, this equals to a spatial pattern of saturated dark magnetic points (Guttman et al., 1994). In figure 1c there is a visual overview of TMR sequences. The grid is oriented at 45 degrees. Notice that some detail is lost in the resulting

TMR image. The spatial pattern of saturated magnetization is applied in the heart's wall at End Diastole (ED). Next, as the heart contracts, the grid deforms accordingly during the cardiac cycle and tissue deformation becomes visible, thus measurable (Fuchs et al., 2004).

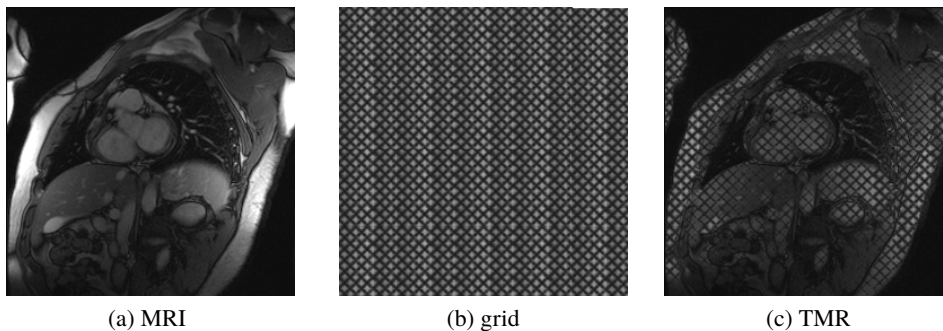


Figure 1: Building a tagged magnetic resonance. Figure 1a is the Magnetic Resonance image. Figure 1b is the SPAMM grid in the image domain. Finally, figure 1c shows the grid overlay over the TMR

MRI devices can be tuned in order to acquire slices in any desired orientation. The standard protocol establishes two slices. These slices are divided according to their orientation with respect to the main axis of the heart, which is the imaginary line from base to apex. Tomographic slices perpendicular to the heart are known as Short Axis (SA) and SA are divided into base, mid and axial cut. On the other hand, Long Axis (LA) views are split into 2-chamber and 4-chamber. In SA cuts, the LV presents an elliptic (almost circular) shape, while its appearance in LA views is U-shaped. Figure 2 shows both LA and SA views, whereas figure 3 illustrates how the TMR sequences look like on each cut.

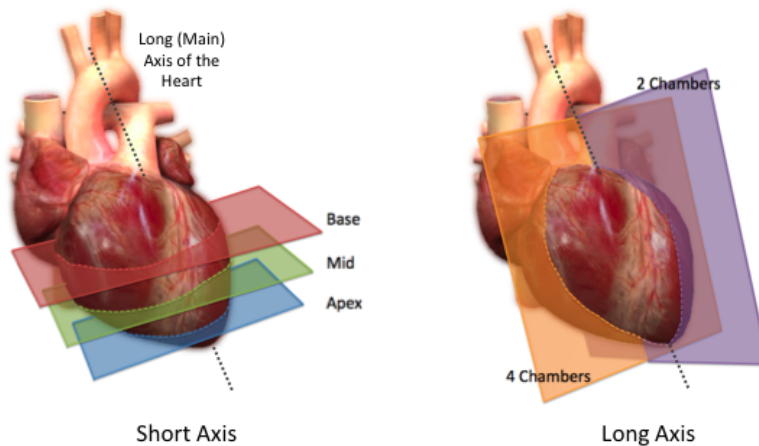


Figure 2: TMR in the standard acquisition views: position of Short-Axis (SA) and Long-Axis (LA) planes.

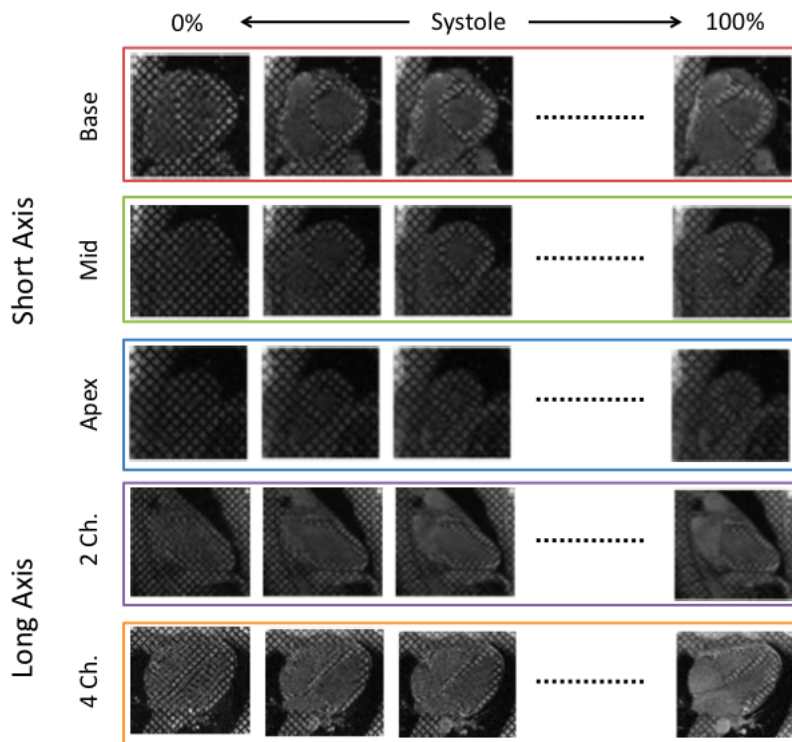


Figure 3: TMR sequences in SA (basal, mid and apical) and LA (2 and 4 chambers) cuts.

## 1.2 Left Ventricle Segmentation

Definition of local scores for assessment of regional wall motion abnormalities requires proper identification of LV segments. The definition of LV segments requires identification of LV boundaries given by its internal (Endocardium) and external (Epicardium) walls. Wall contours can be outlined either manually or by using a computational method. Manual segmentation is accurate as long as there is low inter-observer variability of marked myocardial contours among the manually outlined LV. On one hand, this requires a given segmentation expertise, which is not always available. On the other hand, it is usually a tedious and time consuming task, which invalidates it in systematic clinical practise. Additionally, it is prone to human error, specially after long working hours (Axel et al., 2005). Automatic segmentation is nowadays the preferred method for boundary estimation as it is more efficient than manual approaches, provided that it has a low segmentation error.

Automatic segmentation of LV contours in TMR images is not a trivial task due to the tag pattern, since it misleads common image local descriptors (edges, ridges). Figure 4 shows this artefact. Since TMR places tags on any tissue (muscle, fat), the Canny edges shown in figure 4b detect the tag pattern rather than LV walls, which confuses with LV surrounding tissue. Besides, at early stages of the systole (which is synchronized with TMR sequences acquisition), even blood pool is saturated (Histace et al., 2009), so that it can not be discriminated from tissue (see figure 4a).

The grounds for LV definition were established by the American Heart Association (AHA) (Cerqueira et al., 2002). Their goal was to standardize LV perfusion and function analysis among different image modalities. They proposed a 17-segment model which is a trade-off between anatomical considerations and usability in clinical practise. One common convention for the heart segment is the AHA

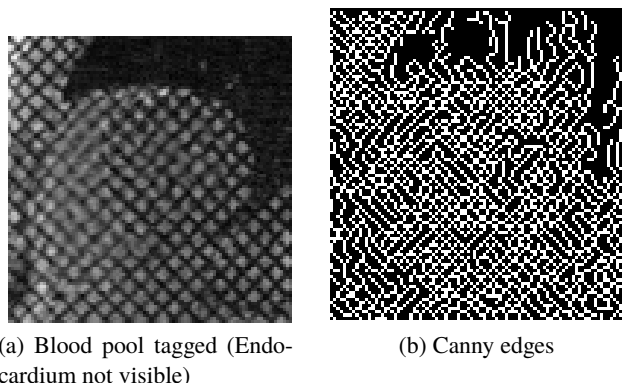


Figure 4: Extracting the contours (figure 4b) from the original TMR sequence (figure 4a) is not possible as the tag pattern misleads common image local descriptors.

model, as seen in figure 5. The AHA segments are the Anterior (A), Anterolateral (AL), Anteroseptal (AS), Inferior (I), Inferolateral (IL) and Inferoseptal (IS) (Cerqueira et al., 2002).

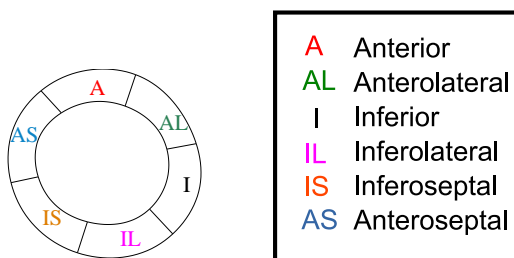


Figure 5: AHA LV sectors for basal and mid cuts. The AHA segments stand for Anterior(A), Anterolateral (AL), Anteroseptal (AS), Inferior (I), Inferolateral (IL) and Inferoseptal (IS).

### 1.3 Main goals

The purpose of this master's thesis is to develop an automatic segmentation method for LV contours in TMR images in SA view at initial acquisition time (End Diastole). Segmentation of the LV at further phases of the cardiac cycle follow from contour tracking (using, for instance, the Harmonic Phase Flow (HPF)-based tracking method developed in Garcia-Barnes et al. (2008)). Our segmentation algorithm has been validated in terms of segmentation error. In order to check its clinical applicability, we have also computed the accuracy of regional scores extracted on the AHA segments defined using our segmented LV contours.

This master's thesis is organized as follows. In section 2, we review earlier approaches for LV segmentation and their suitability for TMR. Next, section 3 describes the process of energy definition and shape correction used in our method for shape segmentation. In section 4, we validate automatic shapes against the ground truth defined by manual segmentations and, also, we explore, for the first time, the impact of segmentation error on the accuracy of regional scores. Finally, in section 5, we discuss the accuracy and robustness of our methods and introduce future lines of work in this area.

## 2. State of the Art

A wide range of methods for LV segmentation in images have been proposed in the literature (Lee et al., to be published; Lynch et al., 2006; Tay et al., 2009; Paragios, 2001). However, many techniques, such as rigid models do not consider the problem of shape deformation. In fact, during the systolic cycle the heart shape varies as it contracts along systole and expands along diastole.

### 2.1 Deformable models

Deformable models are evolving templates that adapt to arbitrary geometries. They are defined a functional including internal and external constrains (Liu and Udupa, 2009). On one hand, the internal energy defines the target object to be segmented. On the other hand, the external energy defines the way that the template is allowed to evolve (elasticity and viscosity). The result is the contour achieving the best compromise between both energies (Milles et al., 2004). In this way an initial shape deforms towards the target contour defined by the external energy, while internal constrains ensure that the final shape does not deviate too much from the preferred shape. In the following parts of this section we review existing deformable models, involved in the segmentation of LV contours.

#### ACTIVE CONTOUR MODELS

Kass et al. (1988) developed Active Contour Models (ACM), also known as snakes. They are curves that segment objects whose boundaries may suffer from a lack of differentiability at the edges or ridges. These elastic curves deform under the influence of external forces while maintaining certain continuity and rigidity constraints determined by internal forces. The balance between internal and external forces is defined so that the ACM conforms to a known boundary, or, in other words, the target shape. Active Contour Models are divided in geodesic and parametric snakes (Chenyang and Prince, 1998).

Geodesic snakes, introduced in Caselles et al. (1995), define snake evolution in the implicit parametrization given by image level-sets. The snake ( $\gamma$ ) is modelled by a Riemannian surface given by the image content (edges). Thus, solving the problem of energy minimization is equivalent to finding the minimum length  $\gamma$  in the Riemannian space. For this, geodesic snakes are defined as steady curves in the form of:

$$\frac{\delta\gamma}{\delta t} = (g\kappa - \langle \nabla I, \vec{n} \rangle) \vec{n}$$

The term  $\langle \nabla g, \vec{n} \rangle$  attracts the snake towards the shape of interest (which should be defined by image edges), while the term  $g \cdot \kappa$  performs like an internal constrain ensuring snake smoothness. Although it also ensures snake motion when the snake is distant from the target object, it might prevent the snake entering into concave parts of the object. One advantage of geodesic snakes is that since they are formulated in implicit level-sets terms, they naturally handle detection of external and internal boundaries in various objects, without resorting to specific contour tracking techniques. However, energy definition requires robust mathematical background and considerable time.

Parametric snakes are explicitly formulated and use Newton mechanics principles for the definition of the internal constrains. A parametric snake is the curve  $\gamma(u) = (x(u), y(u))$  that minimizes

the energy functional:

$$E(\gamma) = \int_{\gamma} (E_{int} + E_{ext}) du = \int \frac{1}{2} [\alpha |\gamma'(u)|^2 + \beta |\gamma''(u)|^2] + E_{ext}(\gamma(u)) du$$

where  $\alpha$  controls elasticity and  $\beta$  rigidity. The internal energy ( $E_{int}$ ) keeps the curve points together (elasticity) while avoiding excessive bending (rigidity). On the other hand, the external energy ( $E_{ext}$ ) attracts the curve points towards the desired image edges. Usual external energies include the image gradient:

$$g = \frac{1}{1 + |\nabla u|^2}$$

or the distance map to image edges. The first criteria is not suitable for binary images, as the tensor map is almost flat, which means that the snake remains static. Distance maps are better suited for binary images of edges since distance is defined for each pixel. Hence, at every point of the map the snake experiences attraction towards them. The solution to the former equation is computed using an iterative scheme given by the minimum energy. This minimum energy is reached when:

$$\alpha \gamma''(u) - \beta \gamma''''(u) - \nabla E_{ext} = 0$$

The previous equation means that the snakes will converge in the opposite direction of the external energy vector field orientation.

Summarizing, ACM iteratively evolve an initial curve (set of points) from an initial position to the target shape by virtue of this balance between external and internal energies. However, there are some issues that make simple parametric snakes unsuitable for image segmentation. First, unless the initial snake is placed close to the target boundary it is unlikely to converge to the real solution. Moreover, boundary concavities could trap the snake and stop the evolution process unless we define appropriate gradient vector flows (Giraldi et al., 2005). Also, few a priori knowledge about the shape to segment can be incorporated, except for minor parametric adjustments controlling elasticity and rigidity (van Ginneken et al., 2002). Fortunately, Active Shape Models (ASM) can overcome this last drawback.

#### ACTIVE SHAPE MODELS

Active Shape Models were proposed by Cootes et al. (1995) in order to address shape segmentation in medical images. The main difference from ACM is that the internal energy is given in terms of similarity to a template of the target anatomical structure. The template might be either a simplified representation of the organ (given by a simple primitive) or an average shape learnt from a training set of images, the Point Distribution Models (PDM) (Hamarneh et al., 1998). The main difference is that the snakes have a limited range for evolution. This allows ASM to segment the desired object while allowing some variability in the target shape, which is the case of our LV boundaries. In this last case, the desired shape is represented by a set of labelled points (or landmarks). Each point is related to an anatomical feature in the image.

Building the PDM is a three stage process. First, points on the training shapes are identified (usually manually) in a predetermined order. Second, since the anatomy is independent of size and point of view, shapes are aligned in order to remove affinities. This way, the resulting shapes have the same orientation, scaling and rotation. Finally, the variability of shapes is modelled using Principal Component Analysis (PCA).

## 2.2 Segmentation of TMR images

In the literature, there are several methods for automatic segmentation applied to magnetic resonance images (Chen et al., 2009; da Silva Oliveira and Dias, 2007). However, few deal with TMR image issues, mainly because tag properties are similar to those of the target boundaries which hinders the segmentation process. Besides, at End Diastole, the blood pool is also tagged, therefore, the myocardial boundary is not visible. Indeed, existing approaches take special care in the definition of the external energy

The early approach of Guttman et al. (1994) is a complex multi stage process combining mathematical morphology, MR signal models, template matching, dynamic programming, and a priori knowledge of the shape of the LV. However, it is only used in radial/parallel tag patterns (not matrix patterns) and error correction from blood pooling is done manually using a graphical user interface. Therefore this process is not fully automatic and still requires human expertise. Milles et al. (2004) introduces a three stage algorithm which takes into account motion information. First, a pre-processing stage computes the motion fields of the initial frame of the image sequence. Next, a template is initialized and then used for segmentation by applying geometric models and a specially designed potential image. Finally, the remaining frames are estimated using the reference frame and motion fields. After that, a very recent work by Histace et al. (2009) integrates contour and texture analysis for a better global segmentation. Due to blood circulation between two contraction, the tags fade away at certain parts of the image. Thus, the author argues that it is possible to discriminate the myocardial boundaries with local texture parameters for each part.

## 2.3 Our approach

This master thesis proposes an automatic segmentation of the LV in TMR sequences. Our approach is based in the classic formulation of snakes built on the minimization of external and internal energies. The external energy models the target shape we want to segment, while the internal energy imposes constrains on the shape deformation and geometry. Tissue can be semantically described as those parts of the image that are tagged along systole and experience a significant (compared to surrounding static tissue) deformation along systolic cycle. The external energy is obtained by translating the former description into mathematical terms. Regarding internal energy we impose regularity constrains and a prior knowledge of LV contours shape learned from manual segmentations of a training set of MRI sequences. From this training we compute shape model which represents the mean shape and the variation modes of all instances. In order to relax the numeric scheme and reduce the computational cost, shape constrains are forced after snake convergence following ASM.

### 3. Our contribution

As stated in the previous section, conventional segmentation methods are ill-posed for LV contour detection. Although ACM provide smooth curves, they are prone to get stuck in local minima unless initialize close to the target contour. This is compensated in ASM by the a priori knowledge of the target shape, which ensures convergence to a shape close to the target one. However a major inconvenience is the increase in complexity introduced by the a priori shape constrain.

Inspired in Garcia i Barnès (2004), our strategy for LV contour segmentation is a two-fold process. First, in the segmentation step we use Snakes that deform under a potential tailored for TMR images. Next, the correction stage uses ASM after Snake convergence in order to correct any deviation from the desired result. Please note that for each axial cut we requires a corresponding training set. This is due to the fact that the geometry of the LV is different in both cases. Consequently, we will correct the LV shape using the corresponding mean shape model for that cut.

#### 3.1 Segmentation stage

Classic Snakes evolve under the influence of two energies. The internal energy controls elasticity and rigidity which is fairly standard. Moreover, it as a standard formulation in terms of the Snake first. Concerning external energy, it attracts the Snake towards the desired boundaries. Regarding this part, although standard potentials are available in the literature, several others can be synthesized depending on the problem. In our case we define a potential which agrees to the appearance of LV in TMR sequences.

First of all, we provide a semantic description of our object of interest. We define the LV as those areas in the image which present a well defined tag pattern along the whole systolic cycle and any amount of motion. Figure 6 illustrates the former features for a pixel in the LV (green circle), a background pixel (bellow circle) and a pixel on surrounding tissue (red circle). We show the position of such pixel for three shots of the TMR sequence. The position of the pixel on the LV varies across frames, as the heart beats, and it keeps tags for all frames. Surrounding tissue also keeps tags along systole but it is motionless. Finally, the background pixel presents neither tags not motion.

In order to mathematically formulate the semantic descriptors, we will base them in the Harmonic Phase Flow for tissue tracking described in Garcia-Barnes (2006). Harmonic Phase Flow is a variational method for time tracking, specially designed for TMR sequences. It is based on the response of a couple to Gabor Filters banks (A et al., 2004). The combination of the response of both filter banks produces a complex image whose phase is related to tissue motion. In figure 7 we can see the systolic cycle and the associated Gabor filter bank response amplitude and phase images. Furthermore, the amplitude indicates which areas of the image present a reliable tag pattern. Thus, it detects, for each frame, the tagged tissue. On the other side, the module of the vector field provided by HPF measures the amount of motion undergone by each pixel at a given frame. In order to obtain a single measure of tagging pattern and motion, amplitudes and modes for all frames should be combined. Since the values obtained for a given pixel might not correspond to the same anatomical point (especially at moving areas), motion should be compensated first. We use HPF to backtrack any quantity (either amplitudes or module) to the first frame (HPF-based registration).

We will denote by  $\{\lambda_1^t\}_{t=1}^T, \{\lambda_2^t\}_{t=1}^T$ , the amplitudes of the two Gabor filter banks obtained for a sequence of T frames backtracked to the first frame. Also, let  $\lambda_{HPF}^t$  be the HPF module backtracked to the first frame. We define two energy potentials ( $E_1$  and  $E_2$ ) for segmentation.  $E_1$  is the product of the mean ( $\mu$ ) sequence of the HPF module and the mean amplitude in both directions.

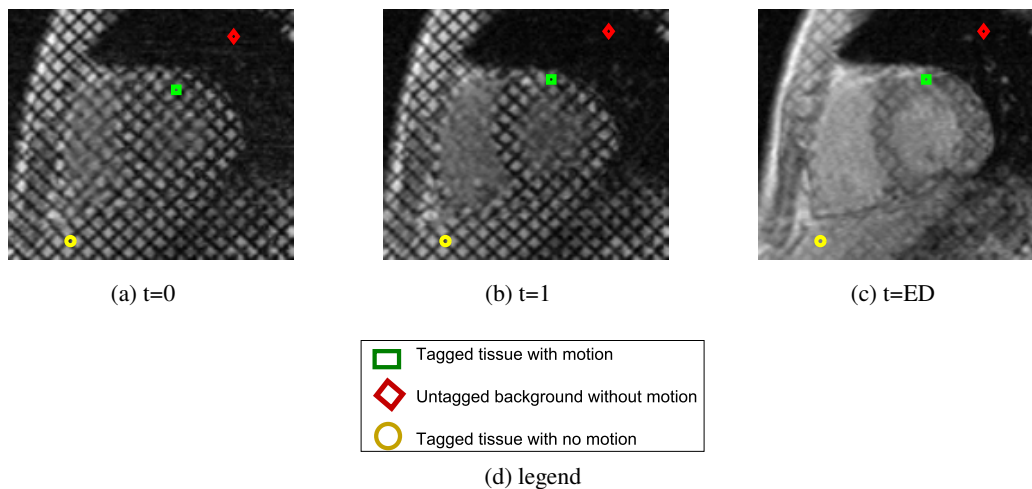


Figure 6: Evolution of the LV features for a pixel in the beginning (figure 6a), the immediate frame 1 (figure 6b) and the last frame (figure 6c).

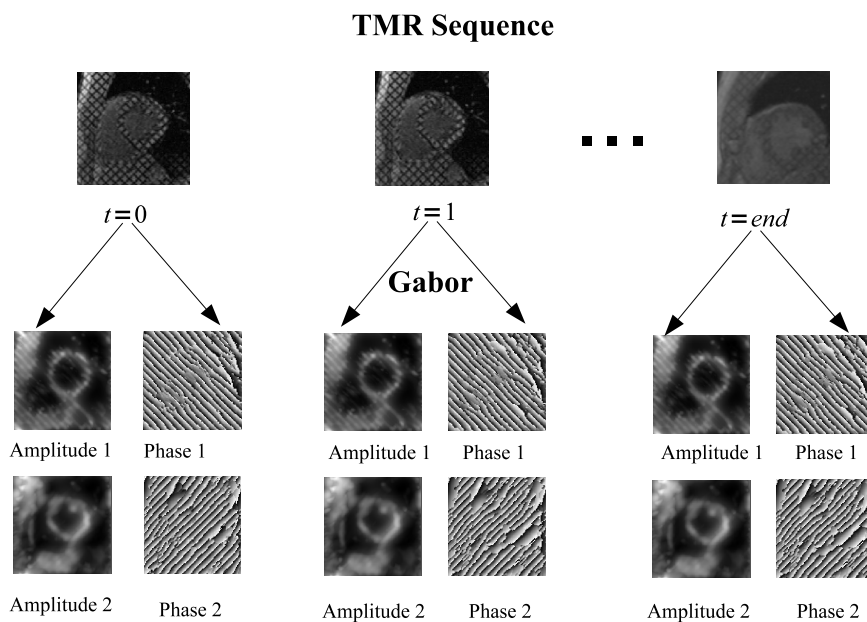


Figure 7: Extraction of the amplitude and phase Gabor in the TMR sequence. Each frame in the original sequence has two complementary amplitude and phase images. The amplitude images filter the tags of the original sequence.

For the definition of  $E_2$ , we combine all three sequences ( $\{\lambda_{HPF}\}_{t=1}^T, \{\lambda_1^t\}_{t=1}^T, \{\lambda_2^t\}_{t=1}^T$ ) into a

single one and then we compute its mean. The formulation of the two potentials  $E_1$  and  $E_2$  is:

$$E_1 = \text{mean}(\text{Amplitude1}) \cdot \text{mean}(\text{amplitude2}) \cdot \text{mean}(\text{HPF}) =$$

$$\mu(\{\lambda_1^t\}_{t=1}^T) \cdot \mu(\{\lambda_2^t\}_{t=1}^T) \cdot \mu(\{\lambda_{HPF}\}_{t=1}^T)$$

$$E_2 = \text{mean}(\text{Amplitude1} \cdot \text{Amplitude2} \cdot \text{HPF}) = \mu(\{\lambda_1^t\}_{t=1}^T \cdot \{\lambda_2^t\}_{t=1}^T \cdot \{\lambda_{HPF}\}_{t=1}^T)$$

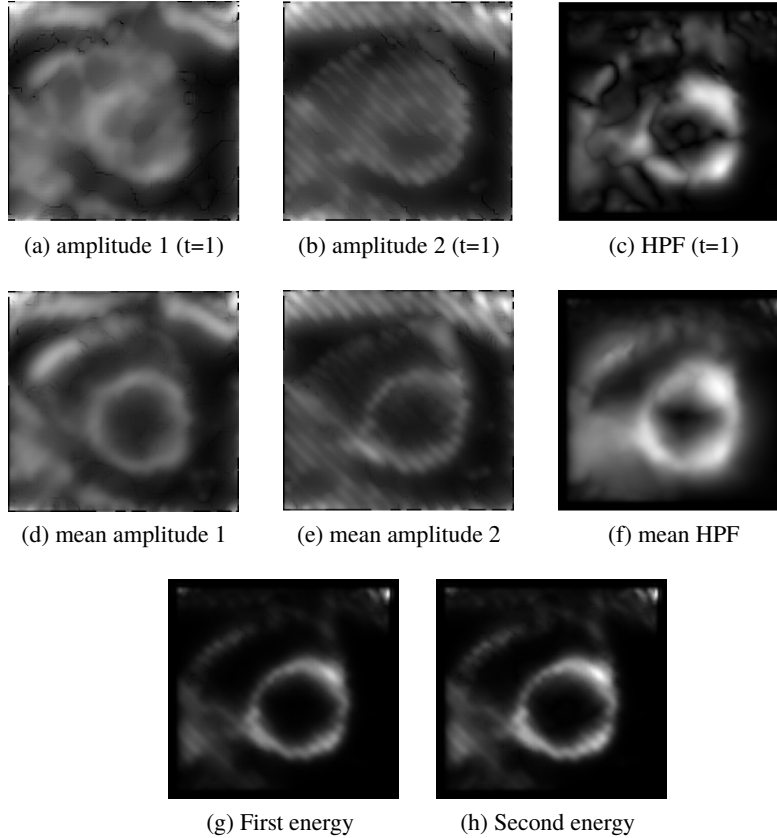


Figure 8: Image sequences for amplitudes  $\lambda_1$ ,  $\lambda_2$  (figures 8d,8e) and the HPF  $\mu(\{\lambda_{HPF}\})$  (figure 8f). The convolution of the three mean sequences defines the first energy potential  $E_1$ . Figures 8a,8b show the first frame of the amplitude of the gabor sequence. Similarly, figure 8c shows the first frame of the HPF module. The combination of 8c,fig:gfm1 and 8b results in  $E_2$  (figure 8h)

Figure 8 shows the descriptors of myocardial tissue and the two energies that we have considered. Although any of the two energies define LV contours as maximum values, the response is not uniform along myocardial tissue. Therefore, we require an additional Structure-Preserving Smoothing (SPF) stage in order to bring the contour patches closer. Gil et al. (2009) argues that for incomplete level curves, the effect of distributing heat makes the curve evolve towards a closed contour of uniform grey level. The effect is an image with smoother transition between gradient intensities.

The final result is an presenting a bimodal distribution where the brightest points correspond to the LV domain. In figure 9c, we segment such points by applying a two k-means clustering (Cheung,

2003) followed by a dilation with a diamond-shaped kernel. This way, we ensure closed contours and remove small structures. Canny edges of the dilated image include myocardial contours. Figure 9 shows the main steps of the process.

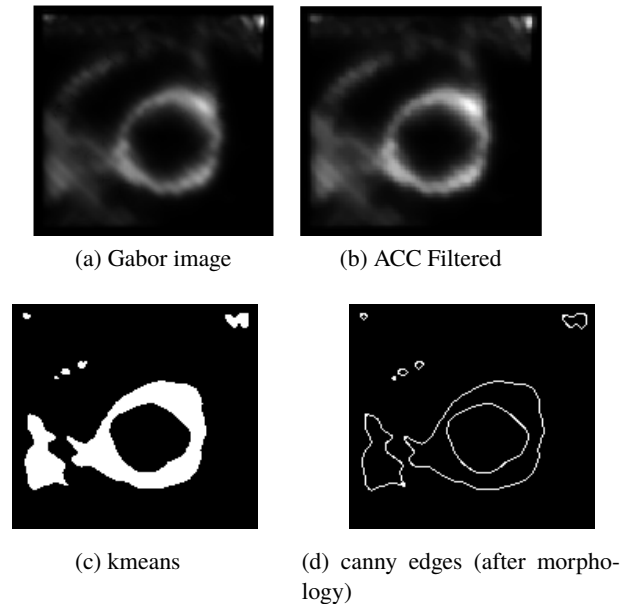


Figure 9: Edge detection and closing. The amplitude image intensity is smoothed using SPF (9b). Next, kmeans (9c) segments the image by clustering each pixels according to its intensity, which serves for background subtraction. After this, the canny edge detector combined with binary morphology (Narayanan et al., 2006) operations returns the candidates for LV edges (figure 9d).

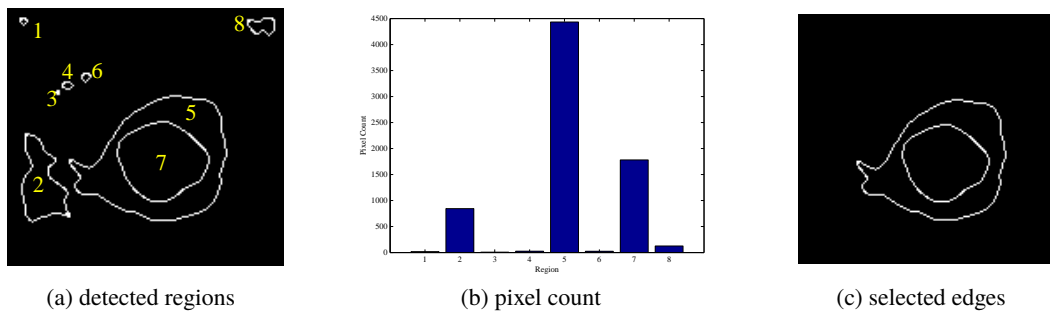


Figure 10: Filtering the detected edges for external energy definition. Figure 10a shows the filled pixel area of each edges. Next, figure 10b shows the total amount of pixels per zone. Finally, the selected edges are shown in 10c. Notice that the Endocardium (the external boundary in figure 5 ) is assumed to be located within the Epicardium (internal boundary, region 7).

Figure 10 illustrates the selection of endocardial walls from the original set of Canny edges of k-means clustering. Left Ventricle borders are selected by curve length and inner region pixel filling. Basically, we count the number of pixels within the closed region formed by the curve. The two

largest pixel counts belong to the Epicardium and Endocardium respectively. We do not filter the curves by length, as in some cases the two longest curves might correspond to large areas with few pixels, or even curves that are not closed. The distance map to each of the contours (Endocardium and Epicardium) are the external potentials used for separately driving two snakes, one for each LV wall. As in ASM, the initial snakes are given by the average template computed for the shape correction. In order to ensure convergence the snake parameters  $\alpha$  and  $\beta$  have been carefully selected. After convergence we correct the set of the two snakes as follows.

### 3.2 Shape Correction Stage

To overcome the problem of the snake being stuck in local minima, we use ASM in order to learn the expected appearance of the final result. We impose this a priori knowledge to the converged snake to improve the segmentation performance.

#### LEARNING THE LV SHAPE

Since the tag pattern hinders a proper visualization of LV boundaries for learning the LV shape, we use untagged MRI images (where the LV is fully visible) as the training set. Given a training set of  $N$  instances, the first step for shape learning is to select a suitable set of landmarks. These landmarks represent the overall shape. More importantly, all landmarks must refer to the same anatomical location in all instances of the training set.

We proceed in the following manner. First, we approximate the LV centroid. Next, we select the Right Ventricle (RV) and LV junction point at the anterior wall in both the Epicardium and Endocardium. Finally, we select  $M$  points in the Epicardium and Endocardium that are circumferentially equally distributed. Refer to figure 11 for the acquisition of points.

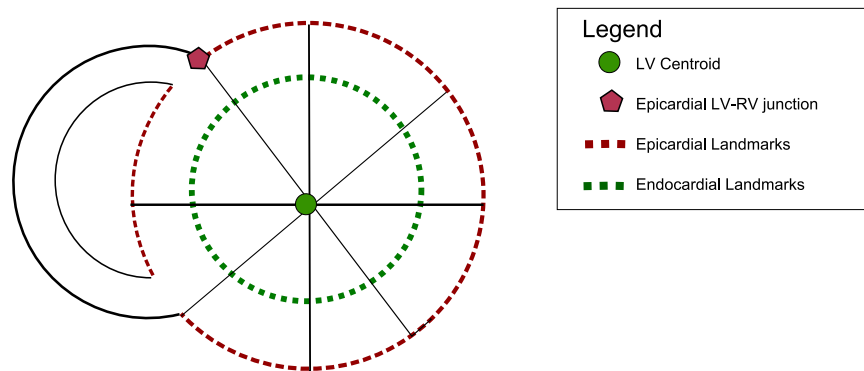


Figure 11: An sketch of the parametrization process. The LV-RV junction is selected first. Starting from there, we choose up to  $M$  points of each boundary (Epicardium and Endocardium) in a circular distribution.

In order to model the intrinsic shape variation between the individuals in the training set, any affinities among them should be removed. This follows from the fact that any anatomical shape is independent of its size, rotation and translation. Affinity removal is achieved by means of Generalized Orthogonal Procrustes Analysis (GOPA) (Gower, 1975). Figure 12 shows the training set before (on the left) and after (on the right) GOPA alignment.

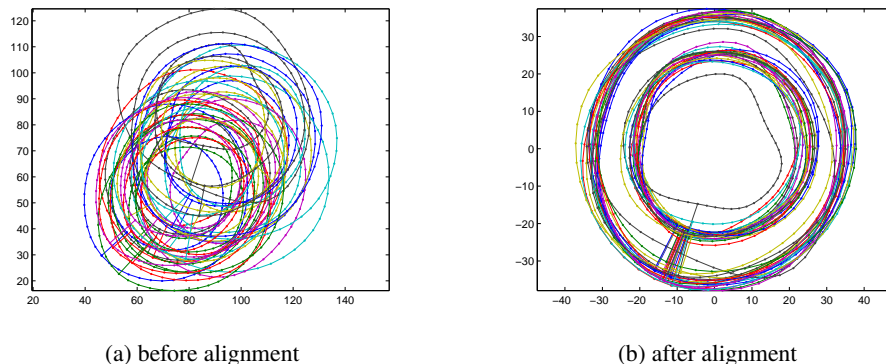


Figure 12: Procrustes alignment of the training set. By removing the differences in translation, rotation and scaling, shape correspondence is now possible.

Once the shapes are aligned we assume them to follow a Gaussian-like distribution. Let  $X_n$  denote the  $n$ -th shape. For each instance of the training set, we represent the mean shape of the LV by concatenating the components of all landmarks in a single feature vector, denoted by  $X_n$ , for the subscript indicating a sample in the training set. That is, if we have  $m$  points for each LV wall, namely  $\{(xED^i, yED^i)\}_{i=1}^m$  for Endocardium and  $\{(xEP^i, yEP^i)\}_{i=1}^m$  for Epicardium, our feature vector is:

$$X_n = (xED_n^1, \dots, xED_n^m, yED_n^1, \dots, yED_n^m, xEP_n^1, \dots, xEP_n^m, yEP_n^1, \dots, yEP_n^m)$$

The shape model is obtained from the feature vector by finding the mean ( $\bar{X}$ ) and the covariance matrix of the training set( $S$ ):

$$\bar{X} = \frac{1}{N} \sum_{n=1}^N X_n$$

$$S = \frac{1}{(N-1)} \sum_{n=1}^N (X_n - \bar{X})(X_n - \bar{X})^T$$

The eigenvectors of the matrix  $S$  (which will be noted by  $\phi_n, n = 1 \dots 4m$ ) represent the modes of variation of the average model. Meanwhile, the associated eigenvalues (which will be noted by  $\lambda_n, n = 1 \dots 4m$ ) indicate the relevance (in terms of energy) of such mode. Dimensionality reduction is attained by resorting to the most relevant modes of variation (principals components). The metric for this relevancy is the total variance described by each eigenvector. Indeed, the eigenvalues serve for this purpose (relevancy). For this reason, the number of selected eigenvectors  $d$  is such that the model represents a maximum percentage ( $prc$ ) of the total variance given by the sum of all eigenvalues:

$$\sum_{n=1}^{4m} \lambda_n$$

Therefore, if we sort eigenvalues in decreasing order (that is,  $\lambda_n \geq \lambda_{n+1}$ ),  $d$  is the smallest number such that:

$$\sum_{n=1}^d \lambda_n \geq \frac{prc}{100} \sum_{n=1}^{4m} \lambda_n$$

Each shape  $X_n$  in the training set can be approximated by a projection into the subspace generated by  $\{\phi_n\}_{n=1}^d$  given by the formula:

$$X_n = \bar{X} + \Phi b_n$$

where  $\Phi$  is a  $4m \times d$  matrix given by the column vectors  $\phi_1, \dots, \phi_d$  and  $b_n = \Phi^\perp(X_n - \bar{X})$  are the components of the projected vector.

The modes of variation also allow the generation of new shapes which agree to an expected anatomy for the LV by varying the coefficients  $b = (b_1, \dots, b_d)$  within a suitable range. Under the assumption of Gaussianity, the range  $[-2\sqrt{\lambda_n}, +2\sqrt{\lambda_n}]$ , represents  $\pm 2$  standard deviations along the mode. It follows that shapes with higher coefficients should be consider abnormal. Figure 13 shows how modifying  $b_n$  creates new shapes within the limit.

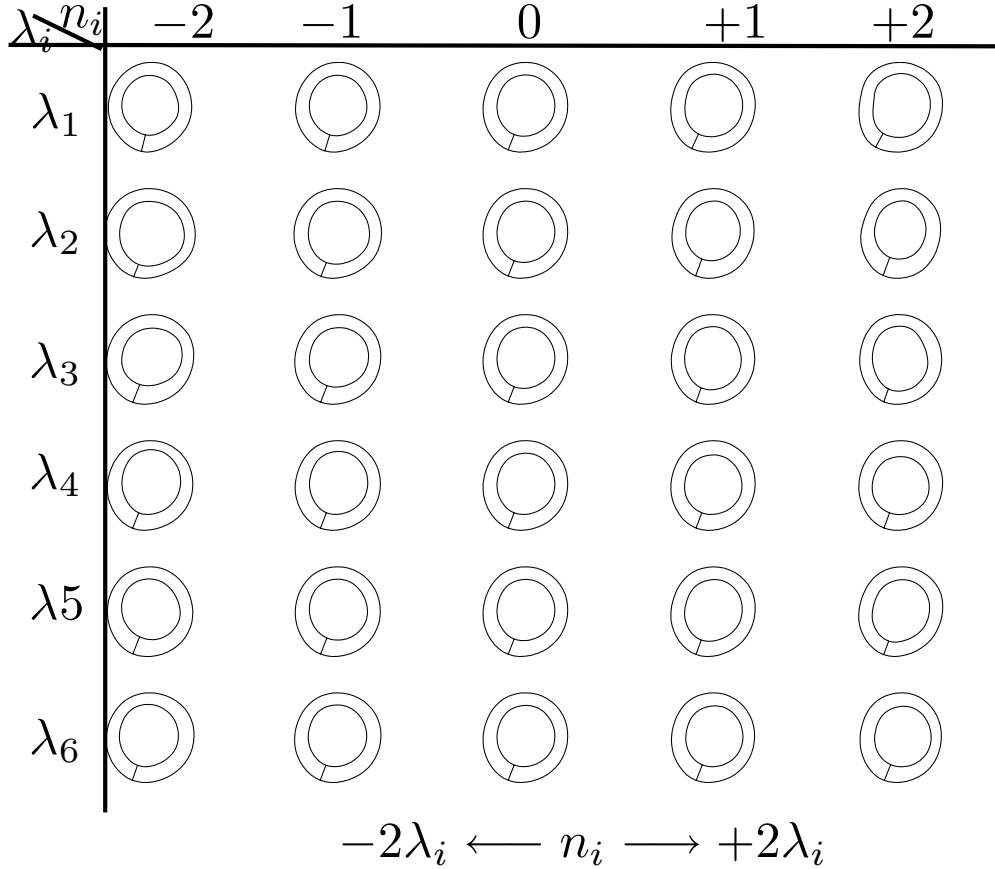


Figure 13: The first six modes of variation illustrate how each of them can generate new shapes from the mean model. The mean shape is located in the middle column. In our study, we conclude that this amount modes are sufficient for representing  $> 95\%$  of the total energy of the training set.

## CORRECTING THE SHAPE

After convergence of the snake, we correct its shape as follows. Firstly, key points are considered from the incoming shape. Next, using GOPA, we compute the affine transform that aligns the input with the mean shape. After this, we project the aligned shape into the PCA space, in order to obtain a valid shape as similar as the incoming shape. Finally, we apply the inverse of the affine transformation in order to place the corrected shape into the image domain. The shape correction process is sketched in figure 14.

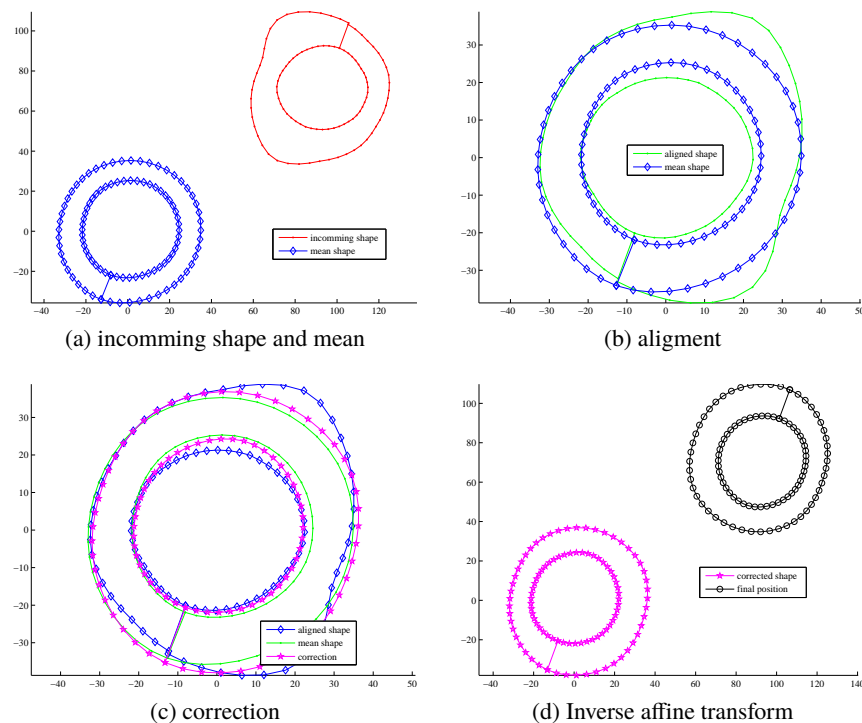


Figure 14: Steps for shape correction. Initially (14a), the incoming shape and the mean shape are not aligned. Therefore, in figure 14b, the input shape is aligned with the mean shape using Procrustes analysis. After this, the shape is projected into the PCA space (figure 14c) and the modes of variation are restricted to  $\pm 2\sqrt{\lambda_n}$ . Finally (figure 14d), the corrected shape is translated back into the original incoming shape position by means of an inverse affine transform.

### 3.3 TMR Segmentation

On the other hand, the internal energy is controlled by the snake parameters found in table 1. In the case of mid axial cuts, the snake convergence requires more influence of the gradient vector flow (figure 15) generated from the distance map to the edges owing to the intrinsic shape of the segmentations.

In order to initialise the snakes close to the final solution we use the original mean shape of the PDM as the initial snake. Using GOPA, the mean shape is aligned towards the filtered edges as seen in figures 16a and 16e.

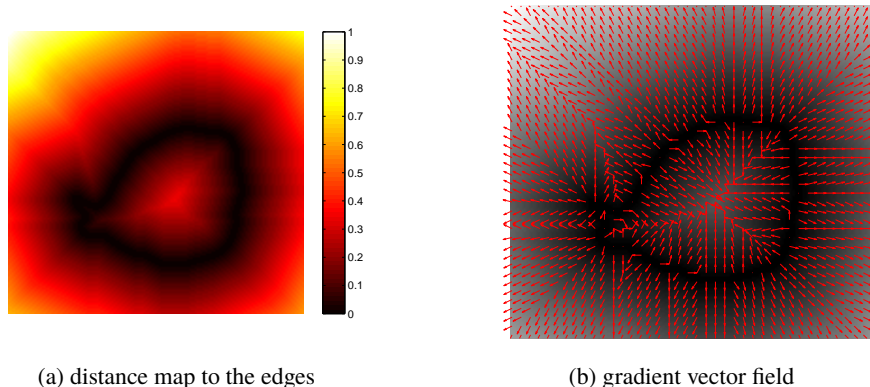


Figure 15: External energy definition using the distance map to the edges (figure 15a) and the corresponding gradient vector field (figure 15b). Intuitively, the edges are the points in the image where the distance is 0. Also, the Snake is attracted in the opposite direction of the field, hence the energies attract the Snake towards the edges.

cut	Elasticity $\alpha$	Rigidity $\beta$	Viscosity $\gamma$	GVF weight $\kappa$
Basal	0.5	0.2	2	1
Mid	0.5	0.7	5	5

Table 1: Parametrization of the internal energy of the snake. Each axial cut requires different parametrizations, since the basal cuts tend to be less noisy.

Figure 16 shows the snake convergence process. In each iteration, the external energy attracts the snakes points towards the desired edges. Meanwhile, the internal energy holds the snake together (elasticity forces) and keep its from excessive bending (bending forces) (Chenyang and Prince, 1998). Thus, snake convergence when is attained when the sum of both energies is minimized. In order to keep point labelling (which is needed for shape registration), we ensure that during convergence the points of the snake do not change their angular order. This is done by deforming the snake using polar coordinates and forcing at each stage the original angular values. The Snake iteration is done separately for the Epicardium and Endocardium.

Once the snake has converged, we correct excessive deviation from the expected anatomies using ASM. Next, we align (affine transform) the converged snake to the average template and consider its coordinates in the PCA space. After this, we apply the shape correction described in 3.2. This way, we avoid excessive deviation from the ground truth while preserving the shape approximation. Finally, we back project into the image domain using the inverse affine transform . Figure 17 shows the snake and the corrected curve. Notice how the snake expands towards the upper right and lower left boundaries. However, the PCA correction draws them back to the target shape.

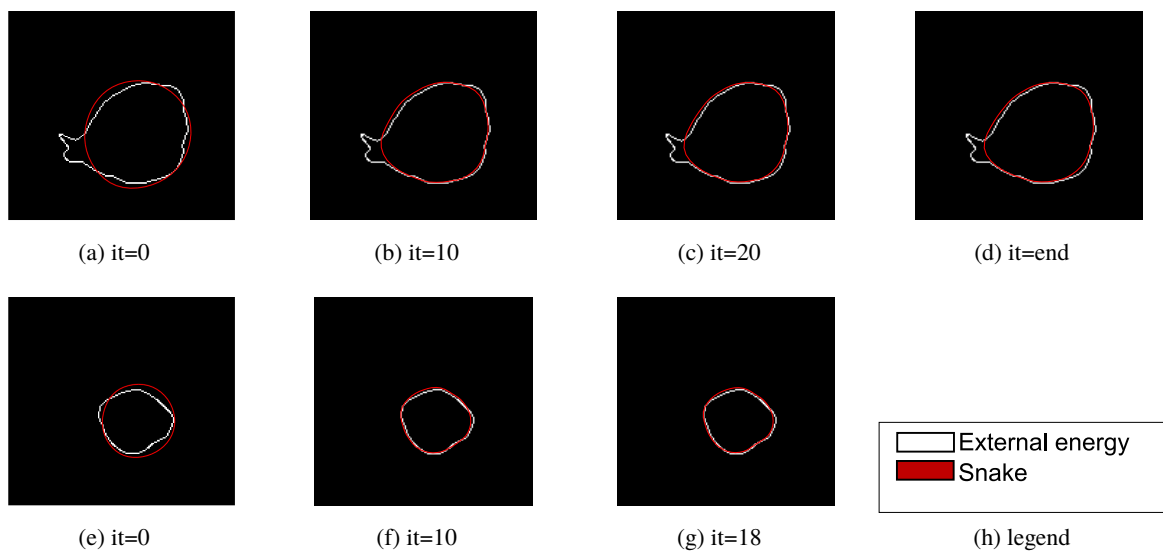


Figure 16: Snake convergence attained with 40 iterations for Epicardium and Endocardium. The initial snake (figure 16a) is placed close to the real boundaries (the external energies). Then, the snake is attracted by the external energy (in white)(figures 16b,16c), until the global energy is minimized (figure 16d). This process is done separately for the Epicardium and Endocardium (figures 16e,16f and 16g).

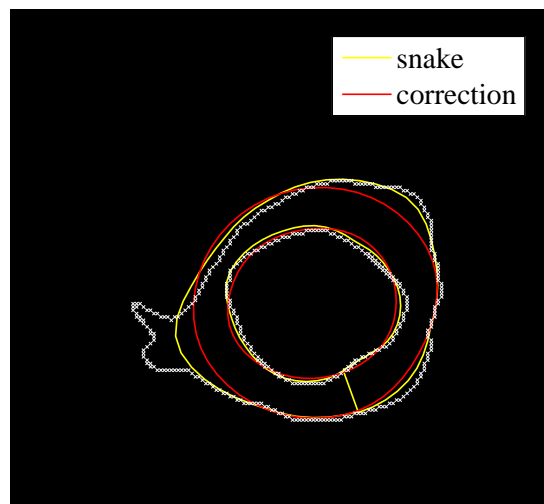


Figure 17: The converged shape is made of the converged Epicardium and Endocardium boundaries. Prior knowledge corrects any excessive amount of deviation from the ground truth.

## 4. Results

Our validation addresses two issues, mainly segmentation error and accuracy of clinical scores. Segmentation error is given by the difference between automated contours and manual segmentations, which constitutes our direct validation procedure. Since the ultimate goal of LV contours segmentation is computing regional scores of the LV function, we have explore the impact of inaccurate segmentations in the computation of such scores. In particular, the global and regional rotation obtained over automated LV domain segmentations has been compared to the values obtained by manually segmenting LV contours. This constitutes our indirect validation procedure.

The automatic segmentation test set has 29 sequences (at mid and basal level) from 15 healthy volunteers. Images were provided by the Clinica La Creu Blanca in Barcelona. When available, we tested the performance of our method in basal and mid cuts on each volunteer. The MRI acquisition was made with a clinical Siemens Magnetom Avanto device. This machine stored the input data in the Digital Imaging and Communication in Medicine (DICOM) interchange format, which is very is common in clinical environments. Additionally, for building the shape model for each cut (basal and mid), we used sets of 21 MRI (non tagged) sequences from 21 healthy subjects. These sequences were landmark by medical experts. This constitutes our ground truth.

Also, the computation of the scores is relative to the physical domain. The DICOM files contain not only the TMR image sequence, but also the equivalent pixel spacing of the image. This value is the physical distance in the patient between the center of each pixel, expressed in millimetres. Thus, we use pixel spacing in order to resize the input image sequence so that each pixel equals to one millimetre. Otherwise the scores would not represent the observed behaviour of the LV.

### 4.1 Segmentation Error

The error between automatic and manual contours has been computed in terms of the Euclidean distance between the two curves. The distance map (image) to manual contours will be noted by  $D_{ED}$  for Endocardium and  $D_{EP}$  for Epicardium. Wwe evaluate distance maps on points sampled over converged snakes. Figure 18a shows distance maps and converged snakes for Endocardium. Next, figure 18b shows the same approach in the Epicardium.

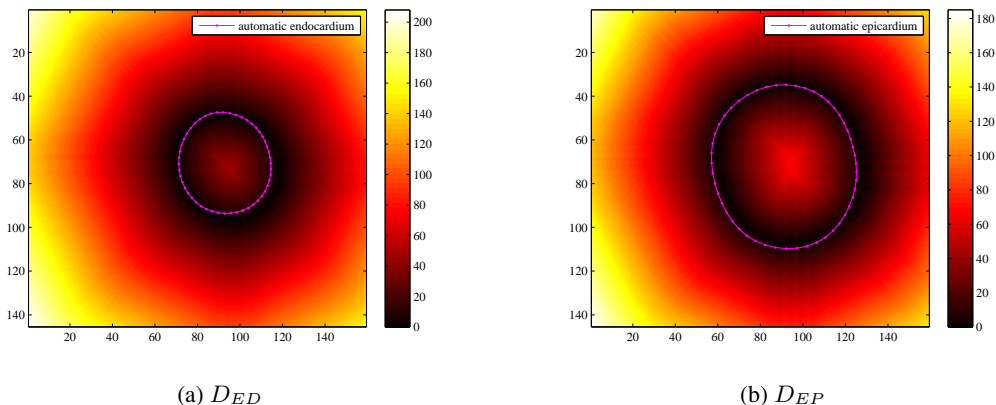


Figure 18: Distance map and automatic contours for endocardium, 18a, and epicardium, 18b.

For each case (which will be noted by the subscript  $n$ ), we have considered the mean ( $\mu_n$ ) and the maximum ( $M_n$ ) values from the distance map. Then, we have computed the data ranges given by the global mean ( $\nu$ ) and the standard deviation ( $\sigma$ ). The distance of all points in both Endocardium and Epicardium are used to compute these quality scores. Also, we recall that one pixel in the image is equivalent to one millimetre.

patient	Basal $E_1$		Basal $E_2$		Mid $E_1$		Mid $E_2$	
	$\mu_n$	$M_n$	$\mu_n$	$M_n$				
1	5.304	11.000	5.098	10.000	4.833	11.000	4.363	11.000
2	11.049	20.000	10.588	18.000	7.108	19.000	6.176	17.000
3	4.235	12.000	4.412	10.000	5.529	14.000	6.500	16.000
4	7.559	16.000	7.657	16.000	7.647	15.000	9.696	22.000
5	-	-	-	-	6.814	16.000	6.392	18.000
6	5.627	12.000	5.275	12.000	10.167	23.000	10.529	23.000
7	-	-	-	-	5.735	18.000	6.010	18.000
8	7.853	15.000	7.657	15.000	7.755	20.000	8.696	21.000
9	-	-	10.559	24.000	6.000	14.000	6.137	13.000
10	-	-	8.225	15.000	6.167	17.000	5.686	15.000
11	7.510	14.000	7.647	16.000	6.461	14.000	6.676	14.000
12	7.235	20.000	7.206	20.000	-	-	-	-
13	6.343	19.000	7.431	29.000	N/A	N/A	N/A	N/A
14	4.765	10.000	4.539	12.000	6.559	18.000	5.461	14.000
15	5.853	13.000	5.990	12.000	5.931	15.000	5.775	14.000
$\nu$	<b>6.667</b>	<b>14.727</b>	<b>7.099</b>	<b>16.077</b>	<b>6.670</b>	<b>16.462</b>	<b>6.777</b>	<b>16.615</b>
$\sigma$	<b>1.801</b>	<b>3.440</b>	<b>1.937</b>	<b>5.370</b>	<b>1.284</b>	<b>3.028</b>	<b>1.701</b>	<b>3.520</b>

Table 2: Statistics from the distance between the manual and automatic shapes in the basal and mid cuts. The results are presented for both energies ( $E_1$  and  $E_2$  (Refer to section 3.1 for more details).  $\nu$  is the global mean,  $\sigma$  the standard deviation

Table 2 reports the quality scores for segmentation error in basal and mid cuts. Each case (labelled patient) is shown on a different row and the two columns correspond to the figures obtained by the two strategies for combining features. The mean error is under 7 millimetres for both energies in all cuts. For basal cuts,  $E_1$  has 73% (11 from 15) valid segmentations. Similarly,  $E_2$  reaches 86% of valid segmentations (13 from 15). On the other hand, since there was no TMR sequence for patient 13 in mid cut,  $E_1$  and  $E_2$  have 93% of valid segmentations (14 out of 15). The dash (-) means that the segmentation process failed to provide a valid LV shape. Unavailable TMR sequences were marked with (N/A).

## 4.2 Accuracy of Clinical Scores

LV rotation is a simple score that recently has gained notorious repercussion in clinical practise, since it relates ejection to filling (Helle-Valle et al., 2005). For each pixel we can define the rotation as the angular difference between the pixel position in current time and End Diastole (Garcia-Barnes et al., 2006). We consider myocardial rotation in two ways, globally and regionally. Global Rotation is obtained considering the whole LV area which is defined by its boundaries. Regional rotation is the mean rotation in each AHA sector of the LV.

For each image in the training set, global and regional rotation curves have been visually assessed. This validates our segmentation method for its systematic use in clinical practise for the extraction of scores such as the rotation. Figures 19, `fig:rotationcomparisongood2` and `fig:rotationcomparisonbad` plot regional rotation at AHA segments (plots labelled (b) to (g)), as well as, global rotations (plots labelled (h)) along systolic cycle. Red curves correspond to automatic rotation profiles and blue ones to manual rotation profiles. Top images show manual (in blue) and automatic (in red) LV region definition super imposed on a TMR frame. Figure 19 show profiles for an accurate segmentation, figure 20 for a moderate error and figure 21i for a segmentation with a significant error.

In figure 19 we see the rotation for an accurate segmentation (basal cut for patient 12). All sector follow the same trend and there is minimal distance between the automatic and manual segmentations. Likewise, the global LV curve is almost identical for both cases.

Figure 20 shows a moderate error between segmentations. In the mid cut of patient 7, the rotation curves diverged in the Anterior (A) sector. The rest were evolved almost identically. The global rotation diverged during half of the systolic cycle, however it followed the same trend (although with considerable distance).

Finally, figure 21 shows a segmentation (mid cut of patient 2) significantly differing from manual contours. Regionally, the rotation curves diverged in all six sectors. The greatest divergence was found in the Anterior (A), Anterolateral (AL) and Anteroseptal (AS) sectors. The rest of the sectors evolved fairly similarly. The global LV rotation diverged in the middle of the systolic cycle.

In tables 3 and 4, we report the difference in regional rotations for automated and manual LV contour identification, for the basal (table 3) and mid (table 4) cuts. The results show that the average absolute error is below one degree. In clinical practise, deviations over one degree are usually not reliable. Moreover, table 5 shows the error in the whole LV region, which is considerable smaller (less than 0.2 degrees) than in the regional scores.

In mid cuts, the average absolute error in each sector is restricted to 1 degrees for both automatic segmentations. Like in basal views, the greatest maximum error is found in the A,AL and AS sectors. Patient 7 is the case with the highest error in the set. Also, since there was no TMR sequence available for patient 13, we could not test our method for this case.

Computing the global rotation of the LV brings more interesting facts about the segmentations. The average absolute mean rotation error is considerably lower than the regional values of basal or mid cuts, way below 0.2 degrees. Furthermore, the greatest deviation is found in the case of in the mid cut for the automatic segmentation 2. In fact, this perturbation is caused by patient 2 again.

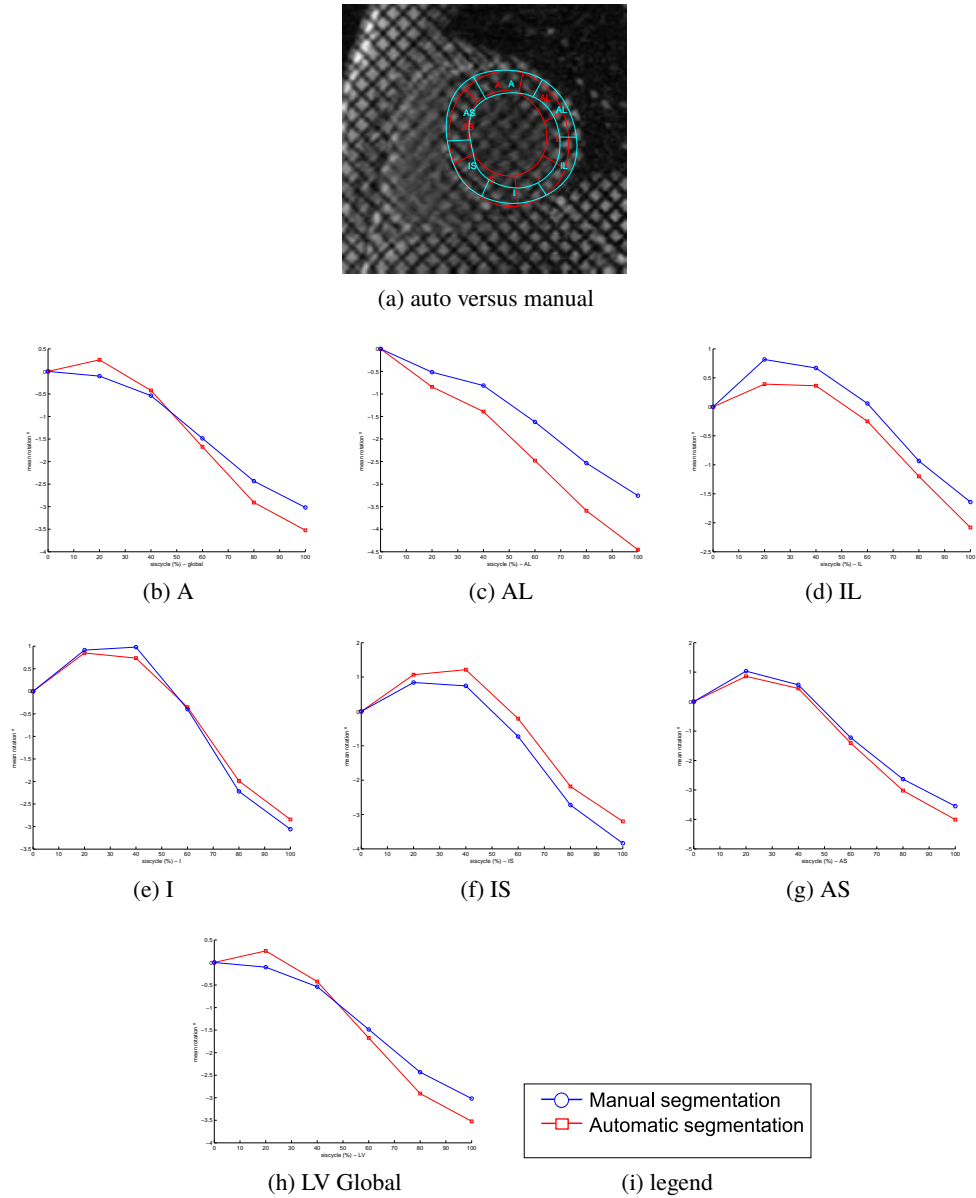
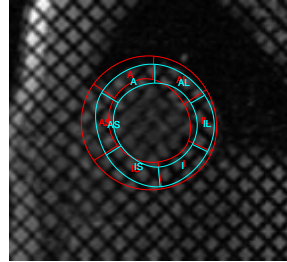
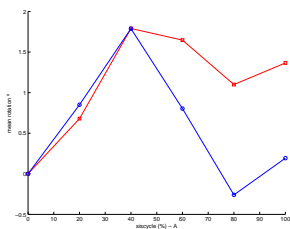


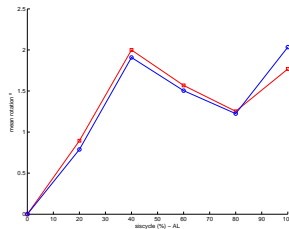
Figure 19: Regional Rotation curves in a good segmentation (figure 19a) in the basal cut (patient 12). Each graphic(figures 19b,19c,19d,19e,19f and 19g) shows the evolution of the rotation at each instant of the systolic cycle until end-Diastole for each sector. The global scores (figure 19h) is also provided for reference.



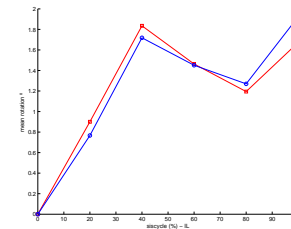
(a) auto versus manual



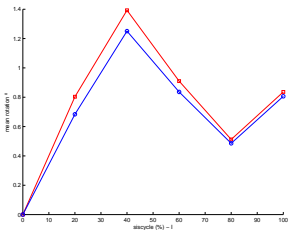
(b) A



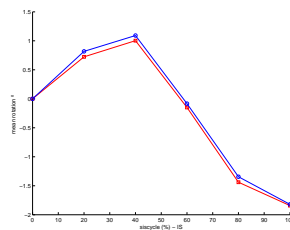
(c) AL



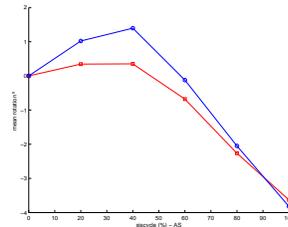
(d) IL



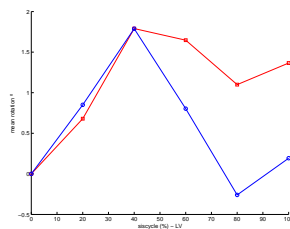
(e) I



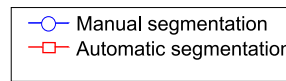
(f) IS



(g) AS



(h) LV Global



(i) legend

Figure 20: Regional Rotation curves in a good segmentation (figure 20a) in the mid cut (patient 7). Each graphic (figures 20b, 20c, 20d, 20e, 20f and 20g) shows the evolution of the rotation at each instant of the systolic cycle until end-systole for each sector. The global scores (figure 20h) are also provided for reference.

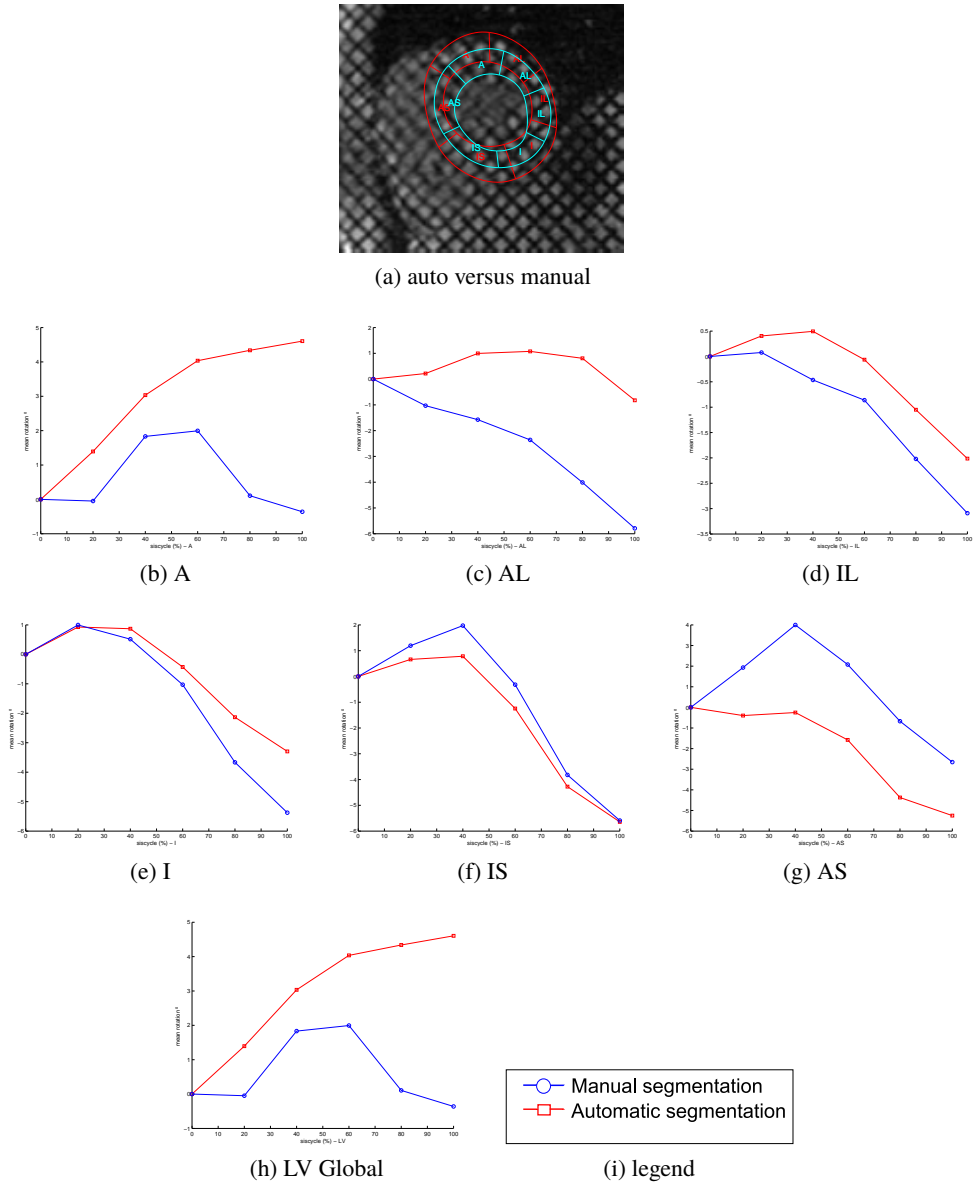


Figure 21: Regional Rotation curves in a bad segmentation (figure 21a) in the mid cut (patient 2). Each graphic (figures 21b, 21c, 21d, 21e, 21f and 21g) shows the evolution of the rotation at each instant of the systolic cycle until end-Diastole for each sector. The global scores (figure 21h) are also provided for reference.

patient	$E_1$						$E_2$					
	A	AL	IL	I	IS	AS	A	AL	IL	I	IS	AS
1	0.343	1.149	0.222	0.144	0.757	0.307	0.262	1.165	0.172	0.181	0.797	0.299
2	2.313	2.839	0.688	0.773	0.526	2.754	2.109	2.780	0.834	0.725	0.471	3.103
3	0.711	1.046	0.451	0.745	0.551	1.547	0.645	0.981	0.526	0.738	0.573	1.555
4	0.649	0.443	0.093	0.069	0.124	0.595	0.703	0.486	0.094	0.066	0.117	0.649
5	-	-	-	-	-	-	-	-	-	-	-	-
6	1.448	0.780	0.134	0.247	0.524	1.027	1.332	0.735	0.149	0.277	0.535	0.858
7	-	-	-	-	-	-	-	-	-	-	-	-
8	0.669	1.627	0.369	0.226	0.221	1.651	0.677	1.660	0.366	0.197	0.216	1.661
9	-	-	-	-	-	-	-	-	-	-	-	-
10	-	-	-	-	-	-	-	-	-	-	-	-
11	1.888	0.283	0.240	0.266	0.472	0.332	1.905	0.297	0.238	0.277	0.467	0.334
12	0.274	0.669	0.291	0.133	0.399	0.220	0.267	0.669	0.312	0.123	0.406	0.207
13	0.124	0.532	0.282	0.748	0.875	0.616	0.292	0.601	0.183	0.681	0.969	0.288
14	0.387	0.809	0.226	0.115	0.269	0.235	0.336	0.788	0.213	0.152	0.269	0.230
15	1.059	0.292	0.223	0.223	0.420	0.358	1.218	0.340	0.216	0.205	0.424	0.368
$\mu$	<b>0.897</b>	<b>0.952</b>	<b>0.293</b>	<b>0.335</b>	<b>0.467</b>	<b>0.877</b>	<b>0.886</b>	<b>0.955</b>	<b>0.300</b>	<b>0.329</b>	<b>0.477</b>	<b>0.868</b>
$\sigma$	<b>0.708</b>	<b>0.742</b>	<b>0.164</b>	<b>0.276</b>	<b>0.221</b>	<b>0.805</b>	<b>0.664</b>	<b>0.720</b>	<b>0.213</b>	<b>0.255</b>	<b>0.246</b>	<b>0.905</b>
min	<b>0.124</b>	<b>0.283</b>	<b>0.093</b>	<b>0.069</b>	<b>0.124</b>	<b>0.220</b>	<b>0.262</b>	<b>0.297</b>	<b>0.094</b>	<b>0.066</b>	<b>0.117</b>	<b>0.207</b>
max	<b>2.313</b>	<b>2.839</b>	<b>0.688</b>	<b>0.773</b>	<b>0.875</b>	<b>2.754</b>	<b>2.109</b>	<b>2.780</b>	<b>0.834</b>	<b>0.738</b>	<b>0.969</b>	<b>3.103</b>

Table 3: Absolute error between manual and automatic segmentations in degrees. The region scores refer to each of the six AHA sectors in the basal cut. The overall statistics include the mean ( $\mu$ ), the standard deviation ( $\sigma$ ), the maxima and the minima for both energies ( $E_1, E_2$ ). In the cases where the rotation was not available (due to incomplete segmentations) it is represented by a slash (-).

patient	$E_1$						$E_2$					
	A	AL	IL	I	IS	AS	A	AL	IL	I	IS	AS
1	0.921	0.841	0.942	0.119	0.984	0.547	0.785	0.889	0.884	0.106	0.958	0.550
2	0.723	0.681	0.245	0.041	1.227	2.045	0.854	0.775	0.208	0.098	0.962	1.742
3	0.345	0.342	0.243	0.054	0.321	0.239	0.211	0.224	0.431	0.142	0.579	0.163
4	0.269	1.010	0.120	0.432	0.443	0.772	0.285	0.903	0.188	0.121	0.073	0.761
5	0.591	0.093	0.098	0.065	0.061	0.447	0.247	0.185	0.122	0.123	0.313	0.457
6	1.204	1.067	0.527	0.179	0.500	2.225	1.266	1.159	0.537	0.179	0.516	2.265
7	0.067	0.275	0.133	0.036	0.043	0.198	0.118	0.193	0.195	0.174	0.046	0.362
8	0.102	0.572	0.245	0.098	1.687	0.921	0.166	0.506	0.398	0.471	2.139	0.998
9	1.203	1.079	0.578	0.454	0.297	1.086	1.170	1.119	0.576	0.438	0.288	1.003
10	0.182	0.425	0.152	0.040	0.206	0.794	0.222	0.451	0.135	0.059	0.145	0.645
11	0.705	0.357	0.245	0.089	0.153	0.299	0.742	0.335	0.228	0.064	0.150	0.319
12	-	-	-	-	-	-	-	-	-	-	-	-
13	N/A											
14	0.122	0.037	0.167	0.506	0.579	0.118	0.150	0.047	0.171	0.323	0.417	0.303
15	0.313	0.124	0.104	0.599	0.396	0.290	0.495	0.213	0.186	0.286	0.186	0.315
$\mu$	<b>0.519</b>	<b>0.531</b>	<b>0.292</b>	<b>0.209</b>	<b>0.531</b>	<b>0.768</b>	<b>0.516</b>	<b>0.538</b>	<b>0.327</b>	<b>0.199</b>	<b>0.521</b>	<b>0.760</b>
$\sigma$	<b>0.405</b>	<b>0.374</b>	<b>0.247</b>	<b>0.208</b>	<b>0.488</b>	<b>0.678</b>	<b>0.403</b>	<b>0.385</b>	<b>0.227</b>	<b>0.138</b>	<b>0.573</b>	<b>0.620</b>
min	<b>0.067</b>	<b>0.037</b>	<b>0.098</b>	<b>0.036</b>	<b>0.043</b>	<b>0.118</b>	<b>0.118</b>	<b>0.047</b>	<b>0.122</b>	<b>0.059</b>	<b>0.046</b>	<b>0.163</b>
max	<b>1.204</b>	<b>1.079</b>	<b>0.942</b>	<b>0.599</b>	<b>1.687</b>	<b>2.225</b>	<b>1.266</b>	<b>1.159</b>	<b>0.884</b>	<b>0.471</b>	<b>2.139</b>	<b>2.265</b>

Table 4: Absolute error between manual and automatic segmentations in degrees. The region scores refer to each of the six AHA sectors in the mid cut. The overall statistics include the mean ( $\mu$ ), the standard deviation ( $\sigma$ ), the maxima and minima for both energies ( $E_1, E_2$ ). In the cases where the rotation was not computable (due to incomplete segmentations), it is represented by a slash (-). Also, when the TMR sequence for that cut was not available was missing it was represented by N/A

	Basal		Mid	
	$E_1$	$E_2$	$E_1$	$E_2$
1	0.009	0.009	0.052	0.054
2	0.405	0.405	0.299	0.263
3	0.068	0.068	0.093	0.082
4	0.067	0.067	0.185	0.188
5	-	-	0.061	0.091
6	0.220	0.220	0.158	0.150
7	-	-	0.073	0.098
8	0.242	0.242	0.156	0.242
9	-	-	0.037	0.039
10	-	-	0.174	0.164
11	0.241	0.241	0.077	0.080
12	0.064	0.064	-	-
13	0.214	0.214	N/A	N/A
14	0.071	0.071	0.173	0.139
15	0.198	0.198	0.235	0.195
$\mu$	<b>0.163</b>	<b>0.163</b>	<b>0.136</b>	<b>0.137</b>
$\sigma$	<b>0.117</b>	<b>0.117</b>	<b>0.079</b>	<b>0.071</b>
max	<b>0.009</b>	<b>0.009</b>	<b>0.037</b>	<b>0.039</b>
min	<b>0.405</b>	<b>0.405</b>	<b>0.299</b>	<b>0.263</b>

Table 5: Absolute error between manual and automatic segmentations of the whole LV (without sectors) in degrees. The overall statistics include the mean ( $\mu$ ), the standard deviation ( $\sigma$ ), the maxima and minima for both energies ( $E_1, E_2$ ). In the cases where the rotation was not computable, it is represented by a slash (-). Also, when the TMR sequence was not available it was represented by N/A.

## 5. Conclusions

We have seen that segmentation in TMR sequences is a challenging task due to the tagging pattern of TMR images. The literature on this subject is limited and non conclusive. Our main contribution is to incorporate motion to the definition of LV points. We semantically define the LV as a texture (grid) deforming during the systolic cycle. This translates into texture analysis with motion estimation in the computational domain. Additionally, prior knowledge from manual landmark segmentations corrects excessive deviation from the ground truth. Thus, our hypothesis is that by combining motion and texture descriptors automatic segmentation could improve.

Our results are consistent with our hypothesis. Empirical evidence in figures 22a and 22b suggests that  $E_1$  and  $E_2$  are suitable external energies for most of the cases. Convergence to the real LV boundaries is observed in the two images. Moreover, in this case, the snake does not expand in the lower right and upper left corners thanks to proper parametrization. In fact, in figure 22b, even if the snake expands below the real boundaries, the shape correction avoid excessive deviation.

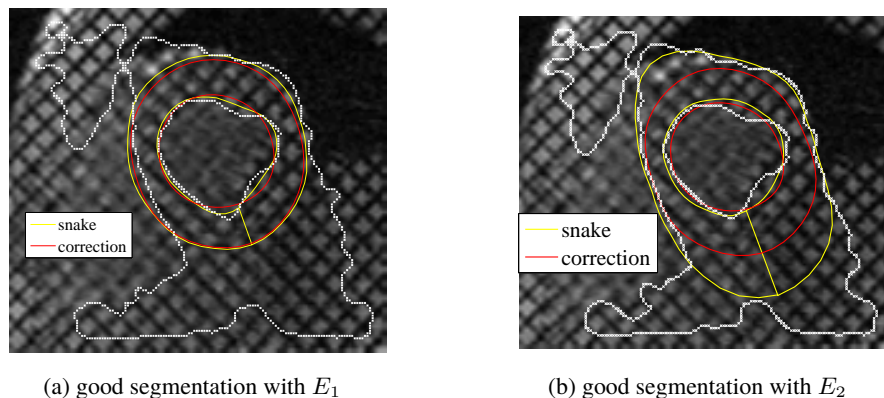


Figure 22: Two good segmentations in the basal cut for patient 14. In figure 22a, we see the results with the first energy  $E_1$ . As for figure 22b, the second energy deformed the snake towards the potential. Nevertheless, in both cases the prior knowledge is able to correct observed deviation from the mean shape.

Still, there were some cases that did not produce valid segmentations. In fact, we could not detect the Endocardium boundary in patients 5,7,9,10 (Basal) and patient 12 (mid). For instance, figure 23a shows the case of the basal cut for patient 5 and the mid cut for patient 12. The most probable cause for this abnormal behaviour is an excessive amount of intensity smoothing by the SPF filter. This filter tends to smooth intensity levels across neighbour regions. If these regions are too close, they may end up having the same intensity. Hence, the canny edge detector considers them as a single region. For this reason, after the k-means, the Epicardium and Endocardium edges may have been fused in the same region. Consequently, the region filtering will fail, as there it will detect a single curve within that region. Since our criteria looks for the Epicardium first, when it searches for the Endocardium, there will not be another candidate region in the image. Thus, the result shall be a single boundary.

As for the rotation LV scores, both automatic segmentations provide similar values, as we have seen in tables 3 and 4. When no scores were available, this was either due to an incorrect definition

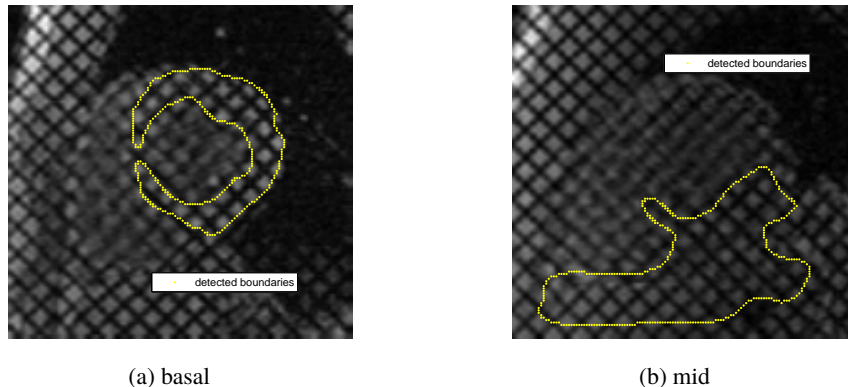


Figure 23: Bad segmentation of the LV boundaries for patient 5 (figure 23a) in the basal cut and patient 12 (mid cut) 23b, both using  $E_1$ . The Epicardium and Endocardium can not be segmented, as both boundaries are joined at some point. Therefore, our method considers this a single curve, and will not find the Endocardium (see section 3.3).

of the external energy ( $E_1, E_2$ ) or because the sequence was not available for that cut (patient 12 mid).

It is also clear that there is a strong correlation between the distance of the automatic and manual LV borders and the computed scores. In other words, the closer they are, the lower the differences in rotation experienced. Nevertheless, our method is robust enough to withstand some amount of deviation in the shape, as the mean error does not exceed one degree on average for all sectors.

In a future line of investigation, we would like to test our method in apical cuts (see section 1.2). We excluded them from our tests since they presented an excessive amount of blur that could not be filtered with the current parametrization of the SPF filter. Thus, the clustering K-Means stage is prone to fail because of the high amount of noise. For this reason, we believe that other techniques, such as Mean-shift (Fukunaga and Hostetler, 1975; Comaniciu and Meer, 2002; Cheng, 1995) might provide improved results. This algorithm seeks the “mode” or point of highest density of a data distribution. Therefore, the segmentation could be given by assigning a low probability to the blood flow and the background.

Additionally, since the HPF can evolve the image points to successive frames, it seems logical to evolve the the automatic segmentation of the LV to the whole systolic cycle (ED). Until now, we have done this until End Systole (ES). However, this will also require the computation of the HPF for all the patients, as the current data only covers the evolution of the myocardium until ED. Likewise, this would enable us to compare our scores with other clinical data extracted with other techniques such as STE.

## 6. Acknowledgements

### Acknowledgments

This project received funding by the Spanish ministerial of Science and Innovation under the Consolider-Ingenio 2010 program MIPRCV (grant number CSD2007-00018). Special thanks to Débora Gil Resina and Jaume Garcia i Barnés for their dedication and support during this master thesis, which played a key role in the development of this master's thesis. We also want to acknowledge the Hospital of Sant Pau for providing their medical knowledge background. Similarly, Clinica Creu Blanca gently provided the TMR sequences used in the test.

The heart short / long axis views (2) and the TMR sequence for each cut (3) are ©Jaume Garcia i Barnés. The UAB logo ©Universitat Autònoma de Barcelona. The CVC logo ©Computer Vision Centre. The consolider logo ©2009 MIPRCV. Other images in this master except previously mentioned ©Albert Andaluz González. All images reproduced with permission of their respective copyright owners.



This work is licensed under the *Creative Commons Attribution-NonCommercial-NoDerivs 3.0 License*. A human readable license is available at [http://creativecommons.org/licenses/by-nc-nd/3.0/es/deed.en\\_GB](http://creativecommons.org/licenses/by-nc-nd/3.0/es/deed.en_GB)

*Help us save the environment. Do not print this document unless strictly needed.*



# References

- Montillo A, Metaxas D, and Axel L. Extracting tissue deformation using gabor filter banks. *In Proceedings of SPIE*, 5369:1–9., 2004.
- Leon Axel, Albert Montillo, and Daniel Kim. Tagged magnetic resonance imaging of the heart: a survey. *Med Image Anal*, 9(4):376–393, Aug 2005. doi: 10.1016/j.media.2005.01.003. URL <http://dx.doi.org/10.1016/j.media.2005.01.003>.
- V. Caselles, R. Kimmel, and G. Sapiro. Geodesic active contours. In *Proc. Fifth International Conference on Computer Vision*, pages 694–699, June 20–23, 1995. doi: 10.1109/ICCV.1995.466871.
- Manuel D Cerqueira, Neil J Weissman, Vasken Dilsizian, Alice K Jacobs, Sanjiv Kaul, Waren K Laskey, Dudley J Pennell, John A Rumberger, Thomas Ryan, Mario S Verani, American Heart Association Writing Group on Myocardial Segmentation, and Registration for Cardiac Imaging. Standardized myocardial segmentation and nomenclature for tomographic imaging of the heart. a statement for healthcare professionals from the cardiac imaging committee of the council on clinical cardiology of the american heart association. *Int J Cardiovasc Imaging*, 18(1):539–542, Feb 2002.
- Bo Chen, Pong C. Yuen, Jian-Huang Lai, and Wen-Sheng Chen. Image segmentation and selective smoothing based on variational framework. *Journal of Signal Processing Systems*, 54(1):145–158, 2009. ISSN 0957-4174. doi: DOI-10.1007/s11265-008-0248-9.
- Yizong Cheng. Mean shift, mode seeking, and clustering. 17(8):790–799, August 1995. doi: 10.1109/34.400568.
- Xu Chenyang and J. L. Prince. Snakes, shapes, and gradient vector flow. 7(3):359–369, March 1998. doi: 10.1109/83.661186.
- Yiu-Ming Cheung. k\*-means: A new generalized k-means clustering algorithm. *Pattern Recognition Letters*, 24(15):2883 – 2893, 2003. ISSN 0167-8655. doi: DOI:10.1016/S0167-8655(03)00146-6. URL <http://www.sciencedirect.com/science/article/B6V15-491J2HM-3/2/4942f54551da6aff6eb7c06a0f6b8d78>.
- D. Comaniciu and P. Meer. Mean shift: a robust approach toward feature space analysis. 24(5): 603–619, 2002. ISSN 0162-8828. doi: 10.1109/34.1000236.

- T. F. Cootes, C. J. Taylor, D. H. Cooper, and J. Graham. Active shape models---their training and application. *Comput. Vis. Image Underst.*, 61(1):38--59, 1995. ISSN 1077-3142. doi: <http://dx.doi.org/10.1006/cviu.1995.1004>.
- W. da Silva Oliveira and A. V. Dias. Interactive left ventricular segmentation in cardiac images. In *Proc. IEEE 11th International Conference on Computer Vision ICCV 2007*, pages 1--6, October 14--21, 2007. doi: 10.1109/ICCV.2007.4409118.
- Esther Fuchs, Markus F Müller, Helmut Oswald, Harriet Thöny, Paul Mohacsi, and Otto M Hess. Cardiac rotation and relaxation in patients with chronic heart failure. *Eur J Heart Fail*, 6(6):715-722, Oct 2004. doi: 10.1016/j.ejheart.2003.12.018. URL <http://dx.doi.org/10.1016/j.ejheart.2003.12.018>.
- K. Fukunaga and L. Hostetler. The estimation of the gradient of a density function, with applications in pattern recognition. 21(1):32--40, January 1975.
- J. Garcia-Barnes, D. Gil, J. Barajas, F. Carreras, S. Pujadas, and P. Radeva. Characterization of ventricular torsion in healthy subjects using gabor filters and a variational framework. In *Proc. Computers in Cardiology*, pages 877--880, September 17--20, 2006.
- J. Garcia-Barnes, D. Gil, F. Carreras, and S. Pujadas. Regional motion patterns for the left ventricle function assessment. In *Proc. 19th International Conference on Pattern Recognition ICPR 2008*, pages 1--4, December 8--11, 2008. doi: 10.1109/ICPR.2008.4761738.
- Jaume Garcia-Barnes. Harmonic phase flow for tissue motion estimation in tagged mr sequences. 2006.
- Jaume Garcia i Barnès. Generalized active shape models applied to cardiac function analysis. Master's thesis, Universitat Autònoma de Barcelona, Building O - Campus UAB,08193 Bellaterra (Barcelona), 2004.
- Debora Gil, Aura Hernandez-Sabate, Mireia Brunat, Steven Jansen, and Jordi Martinez-Villalta. Structure-preserving smoothing of biomedical images. In *13th International Conference on Computer Images and Patterns (CAIP2009)*, 2009.
- Gilson A. Giraldi, Leandro S. Marturelli, and Paulo S. Rodrigues. Gradient vector flow models for boundary extraction in 2d images. In *Computer Graphics and Imaging*, pages 146--151, 2005.
- Céline Goffinet and Jean-Louis Vanoverschelde. Speckle tracking echocardiography, 6 2007. URL [http://www.touchcardiology.com/files/article\\_pdfs/Philips\\_HIRES\[1\].pdf](http://www.touchcardiology.com/files/article_pdfs/Philips_HIRES[1].pdf).
- J. Gower. Generalized procrustes analysis. *Psychometrika*, 40(1):33--51, March 1975. URL <http://ideas.repec.org/a/spr/psycho/v40y1975i1p33-51.html>.
- M. A. Guttman, J. L. Prince, and E. R. McVeigh. Tag and contour detection in tagged mr images of the left ventricle. 13(1):74--88, March 1994. doi: 10.1109/42.276146.
- Ghassan Hamarneh, Rafeef Abu-Gharbieh, Tomas Gustavsson, Rafeef Abu-gharbieh, and Tomas Gustavsson. Review - active shape models - part i: Modeling shape and gray level variations, 1998.

- Thomas Helle-Valle, Jonas Crosby, Thor Edvardsen, Erik Lyseggen, Brage H Amundsen, Hans-Jørgen Smith, Boaz D Rosen, João A C Lima, Hans Torp, Halfdan Ihlen, and Otto A Smiseth. New noninvasive method for assessment of left ventricular rotation: speckle tracking echocardiography. *Circulation*, 112(20):3149--3156, Nov 2005. doi: 10.1161/CIRCULATIONAHA.104.531558. URL <http://dx.doi.org/10.1161/CIRCULATIONAHA.104.531558>.
- Aymeric Histace, Bogdan Matuszewski, and Yan Zhang. Segmentation of myocardial boundaries in tagged cardiac mri using active contours: A gradient-based approach integrating texture analysis. *Int J Biomed Imaging*, 2009:983794, 2009. doi: 10.1155/2009/983794. URL <http://dx.doi.org/10.1155/2009/983794>.
- Michael Kass, Andrew Witkin, and Demetri Terzopoulos. Snakes: Active contour models. *INTERNATIONAL JOURNAL OF COMPUTER VISION*, 1(4):321--331, 1988.
- H Lee, N Codella, M Cham, J Weinsaft, and Y Wang. Automatic left ventricle segmentation using iterative thresholding and active contour model with adaptation on short-axis cardiac mri. to be published. doi: 10.1109/TBME.2009.2014545.
- Jiamin Liu and J. K. Udupa. Oriented active shape models. 28(4):571--584, April 2009. doi: 10.1109/TMI.2008.2007820.
- M. Lynch, O. Ghita, and P.F. Whelan. Left-ventricle myocardium segmentation using a coupled level-set with a priori knowledge. *Computerized Medical Imaging and Graphics*, 30(4):255 -- 262, 2006. ISSN 0895-6111. doi: DOI:10.1016/j.compmimag.2006.03.009. URL <http://www.sciencedirect.com/science/article/B6T5K-4K66F0D-2/2/29790990bac43f4c39ef80c381be36eb>. Medical Imaging and Graphics in SIBGRAPI/SIACG.
- J. Milles, A. van Susteren, T. Arts, P. Clarysse, P. Croisille, and I. E. Magnin. Automatic 2d segmentation of the left ventricle in tagged cardiac mri using motion information. In *Proc. IEEE International Symposium on Biomedical Imaging: Nano to Macro*, pages 153--156, April 15--18, 2004. doi: 10.1109/ISBI.2004.1398497.
- P. J. Narayanan, Shree K. Nayar, and Heung-Yeung Shum, editors. *Computer Vision - ACCV 2006, 7th Asian Conference on Computer Vision, Hyderabad, India, January 13-16, 2006, Proceedings, Part II*, volume 3852 of *Lecture Notes in Computer Science*, 2006. Springer. ISBN 3-540-31244-7.
- Yuichi Notomi, Peter Lysyansky, Randolph M Setser, Takahiro Shiota, Zoran B Popović, Maureen G Martin-Miklovic, Joan A Weaver, Stephanie J Oryszak, Neil L Greenberg, Richard D White, and James D Thomas. Measurement of ventricular torsion by two-dimensional ultrasound speckle tracking imaging. *J Am Coll Cardiol*, 45(12):2034--2041, Jun 2005. doi: 10.1016/j.jacc.2005.02.082. URL <http://dx.doi.org/10.1016/j.jacc.2005.02.082>.
- Nikos Paragios. A variational approach for the segmentation of the left ventricle in mr cardiac images. In *VLSM '01: Proceedings of the IEEE Workshop on Variational and Level Set Methods (VLSM'01)*, page 153, Washington, DC, USA, 2001. IEEE Computer Society. ISBN 0-7695-1278-X.
- Sandra Pujadas, Francesc Carreras, Manel Ballester, Jaume Garcia-Barnes, and Debora Gil. A normalized parametric domain for the analysis of the left ventricular function. In *VISAPP (1)*, pages 267--274, 2008.

Peter C. Tay, Bing Li, Chris D. Garson, Scott T. Acton, and John A. Hossack. Left ventricle segmentation using model fitting and active surfaces. *Journal of Signal Processing Systems*, 55 (1):139--156, 2009. ISSN 0957-4174. doi: DOI-10.1007/s11265-008-0219-1. URL <http://www.springerlink.com/content/8nru61j14179666m>.

Bram van Ginneken, Alejandro F. Frangi, Joes J. Staal, Bart M. ter Haar Romeny, and Max A. Viergever. Active shape models with optimal features. *IEEE TRANSACTIONS ON MEDICAL IMAGING*, VOL. 21, NO. 8, AUGUST 2002, 21:924--933, 2002.

# List of Figures

1	Building a tagged magnetic resonance. Figure 1a is the Magnetic Resonance image. Figure 1b is the SPAMM grid in the image domain. Finally, figure 1c shows the grid overlay over the TMR . . . . .	4
2	TMR in the standard acquisition views: position of Short-Axis (SA) and Long-Axis (LA) planes. . . . .	4
3	TMR sequences in SA (basal, mid and apical) and LA (2 and 4 chambers) cuts. . .	5
4	Extracting the contours (figure 4b) from the original TMR sequence (figure 4a) is not possible as the tag pattern misleads common image local descriptors. . . . .	6
5	AHA LV sectors for basal and mid cuts. The AHA segments stand for Anterior(A), Anterolateral (AL), Anteroseptal (AS), Inferior (I), Inferolateral (IL) and Inferoseptal (IS). . . . .	6
6	Evolution of the LV features for a pixel in the beginning (figure 6a), the immediate frame 1 (figure 6b) and the last frame (figure 6c). . . . .	11
7	Extraction of the amplitude and phase Gabor in the TMR sequence. Each frame in the original sequence has two complementary amplitude and phase images. The amplitude images filter the tags of the original sequence. . . . .	11
8	Image sequences for amplitudes $\lambda_1, \lambda_2$ (figures 8d,8e) and the HPF $\mu(\{\lambda_{HPF}\})$ (figure 8f). The convolution of the three mean sequences defines the first energy potential $E_1$ . Figures 8a,8b) show the first frame of the amplitude of the gabor sequence. Similarly, figure 8c shows the first frame of the HPF module.The combination of 8c,fig:gfm1 and 8b results in $E_2$ (figure 8h) . . . . .	12
9	Edge detection and closing. The amplitude image intensity is smoothed using SPF (9b). Next, kmeans (9c segments the image by clustering each pixels according to its intensity, which serves for background subtraction. After this, the canny edge detector combined with binary morphology (Narayanan et al., 2006) operations returns the candidates for LV edges (figure 9d). . . . .	13
10	Filtering the detected edges for external energy definition. Figure 10a shows the filled pixel area of each edges. Next, figure 10b shows the total amount of pixels per zone. Finally, the selected edges are shown in 10c. Notice that the Endocardium (the external boundary in figure 5 ) is assumed to be located within the Epicardium (internal boundary,region 7). . . . .	13
11	An sketch of the parametrization process. The LV-RV junction is selected first. Starting from there, we choose up to M points of each boundary (Epicardium and Endocardium) in a circular distribution. . . . .	14

12 Procrustes alignment of the training set. By removing the differences in translation, rotation and scaling, shape correspondence is now possible. . . . . 15

13 The first fix modes of variation illustrate how each of them can generate new shapes from the mean model. The mean shape is located in the middle column. In our study, we conclude that this amount modes are sufficient for representing > 95% of the total energy of the training set. . . . . 16

14 Steps for shape correction. Initially (14a) , the incoming shape and the mean shape are not aligned. Therefore, in figure 14b, the input shape is aligned with the mean shape using Procrustes analysis. After this, the shape is projected into the PCA space (figure 14c) and the modes of variation are restricted to  $\pm 2\sqrt{\lambda_n}$ . Finally (figure 14d), the corrected shape is translated back into the original incoming shape position by means of an inverse affine transform. . . . . 17

15 External energy definition using the distance map to the edges (figure 15a) and the corresponding gradient vector field (figure 15b). Intuitively, the edges are the points in the image where the distance is 0. Also, the Snake is attracted in the opposite direction of the field, hence the energies attract the Snake towards the edges. . . . . 18

16 Snake convergence attained with 40 iterations for Epicardium and Endocardium. The initial snake (figure 16a) is placed close to the real boundaries (the external energies). Then, the snake is attracted by the external energy (in white)(figures 16b,16c), until the global energy is minimized (figure 16d). This process is done separately for the Epicardium and Endocardium (figures 16e,16f and 16g. . . . . 19

17 The converged shape is made of the converged Epicardium and Endocardium boundaries. Prior knowledge corrects any excessive amount of deviation from the ground truth. . . . . 19

18 Distance map and automatic contours for endocardium, 18a, and epicardium, 18b. . 20

19 Regional Rotation curves in a good segmentation (figure 19a) in the basal cut (patient 12). Each graphic(figures 19b,19c,19d,19e,19f and 19g) shows the evolution of the rotation at each instant of the systolic cycle until end-Diastole for each sector. The global scores (figure 19h) is also provided for reference. . . . . 23

20 Regional Rotation curves in a good segmentation (figure 20a) in the mid cut (patient 7). Each graphic(figures 20b, 20c, 20d, 20e, 20f and 20g) shows the evolution of the rotation at each instant of the systolic cycle until end-systole for each sector. The global scores (figure 20h) are also provided for reference. . . . . 24

21 Regional Rotation curves in a bad segmentation (figure 21a) in the mid cut (patient 2). Each graphic(figures 21b, 21c, 21d, 21e, 21f and 21g) shows the evolution of the rotation at each instant of the systolic cycle until end-Diastole for each sector. The global scores (figure 21h) are also provided for reference. . . . . 25

22 Two good segmentations in the basal cut for patient 14. In figure 22a, we see the results with the first energy  $E_1$ . As for figure 22b, the second energy deformed the snake towards the potential. Nevertheless, in both cases the prior knowledge is able to correct observed deviation from the mean shape. . . . . 29

23 Bad segmentation of the LV boundaries for patient 5 (figure 23a) in the basal cut and patient 12 (mid cut) 23b, both using  $E_1$ . The Epicardium and Endocardium can not be segmented, as both boundaries are joined at some point. Therefore, our method considers this a single curve, and will not find the Endocardium (see section 3.3). . 30

# List of Tables

1	Parametrization of the internal energy of the snake. Each axial cut requires different parametrizations, since the basal cuts tend to be less noisy. . . . .	18
2	Statistics from the distance between the manual and automatic shapes in the basal and mid cuts. The results are presented for both energies ( $E_1$ and $E_2$ (Refer to section 3.1 for more details). $\nu$ is the global mean, $\sigma$ the standard deviation . . . . .	21
3	Absolute error between manual and automatic segmentations in degrees. The region scores refer to each of the six AHA sectors in the basal cut. The overall statistics include the mean ( $\mu$ ), the standard deviation ( $\sigma$ ), the maxima and the minima for both energies ( $E_1, E_2$ ). In the cases were the rotation was not available (due to incomplete segmentations) it is represented by a slash (-). . . . .	26
4	Absolute error between manual and automatic segmentations in degrees. The region scores refer to each of the six AHA sectors in the mid cut. The overall statistics include the mean ( $\mu$ ), the standard deviation ( $\sigma$ ), the maxima and minima for both energies ( $E_1, E_2$ . In the cases were the rotation was not computable (due to incomplete segmentations), it is represented by a slash (-). Also, when the TMR sequence for that cut was not available was missing it was represented by N/A . . . . .	27
5	Absolute error between manual and automatic segmentations of the whole LV (without sectors) in degrees. The overall statistics include the mean ( $\mu$ ), the standard deviation ( $\sigma$ ), the maxima and minima for both energies ( $E_1, E_2$ ). In the cases were the rotation was not computable , it is represented by a slash (-). Also, when the TMR sequence was not available it was represented by N/A. . . . .	28

# Acronyms

**A** Anterior. 6, 23

**ACM** Active Contour Models. 8, 9, 11

**AHA** American Heart Association. 5, 6, 23

**AL** Anterolateral. 6, 23

**AS** Anteroseptal. 6, 23

**ASM** Active Shape Models. 9--11, 15, 19

**DICOM** Digital Imaging and Communication in Medicine. 21

**ED** End Diastole. 3, 6, 10, 23, 31

**ES** End Systole. 31

**GOPA** Generalized Orthogonal Procrustes Analysis. 15, 18

**HPF** Harmonic Phase Flow. 6, 11, 31

**I** Inferior. 6

**IL** Inferolateral. 6

**IS** Inferoseptal. 6

**LA** Long Axis. 4

**LV** Left Ventricle. 1, 3--6, 8--11, 13--17, 21--23, 30, 31

**MRI** Magnetic Resonance Imaging. 3, 4, 10, 15, 21

**PCA** Principal Component Analysis. 9, 18, 19

**PDM** Point Distribution Models. 9, 18

**RF** Radio Frequency. 3

**RV** Right Ventricle. 15

**SA** Short Axis. 4, 6

**SPF** Structure-Preserving Smoothing. 13, 30

**STE** Speckle Tracking Echocardiography. 3, 31

**TMR** Tagged Magnetic Resonance. 1, 3--6, 10, 11, 21--23, 30, 32

**WHO** World Health Organization. 3